



HAL
open science

Frequency spectrum of the geomagnetic field harmonic coefficients from dynamo simulations

Claire Bouligand, Nicolas Gillet, Dominique Jault, Nathanaël Schaeffer,
Alexandre Fournier, Julien Aubert

► **To cite this version:**

Claire Bouligand, Nicolas Gillet, Dominique Jault, Nathanaël Schaeffer, Alexandre Fournier, et al.. Frequency spectrum of the geomagnetic field harmonic coefficients from dynamo simulations. *Geophysical Journal International*, 2016, 207, pp.1142 - 1157. 10.1093/gji/ggw326 . hal-01451189

HAL Id: hal-01451189

<https://hal.science/hal-01451189>

Submitted on 31 Jan 2017

HAL is a multi-disciplinary open access archive for the deposit and dissemination of scientific research documents, whether they are published or not. The documents may come from teaching and research institutions in France or abroad, or from public or private research centers.

L'archive ouverte pluridisciplinaire **HAL**, est destinée au dépôt et à la diffusion de documents scientifiques de niveau recherche, publiés ou non, émanant des établissements d'enseignement et de recherche français ou étrangers, des laboratoires publics ou privés.

1 **Frequency spectrum of the geomagnetic field harmonic** 2 **coefficients from dynamo simulations**

3 C. Bouligand¹, N. Gillet¹, D. Jault¹, N. Schaeffer¹, A. Fournier², J. Aubert²

¹ *Univ. Grenoble Alpes, CNRS, ISTERre, F-38000 Grenoble, France.*

² *Institut de Physique du Globe de Paris, Sorbonne Paris Cité, Univ. Paris Diderot, CNRS, 1 rue Jussieu, F-75005 Paris, France.*

4 5 **SUMMARY**

6
7 The construction of geomagnetic, archeomagnetic or paleomagnetic field models requires
8 some prior knowledge about the actual field, which can be gathered from the statistical
9 properties of the field over a variety of length-scales and time-scales. However, available
10 geomagnetic data on centennial to millennial periods are too sparse to infer directly these
11 statistical properties. We thus use high-resolution numerical simulations of the geody-
12 namo to test a method for estimating the temporal power spectra (or equivalently the auto-
13 covariance functions) of the individual Gauss coefficients that describe the geomagnetic
14 field outside the Earth's fluid outer core. Based on the spectral analysis of our simulations,
15 we argue that a prior for the observational geomagnetic field over decennial to millennial
16 periods can be constructed from the statistics of the field during the short satellite era. The
17 method rests on the assumption that time series of spherical harmonic coefficients can be
18 considered as realisations of stationary and differentiable stochastic processes, namely or-
19 der 2 autoregressive (AR2) processes. In the framework of these processes, the statistics
20 of Gauss coefficients are well constrained by their variance and one or two time-scales.
21 We find that the time spectra in the dynamo simulations of all Gauss coefficients but the
22 axial dipole are well approximated by the spectra of AR2 processes characterized by only

one timescale. The process parameters can simply be deduced from instantaneous estimates of the spatial power spectra of the magnetic field and of its first time derivative. Some deviations of the Gauss coefficients statistics from this minimal model are also discussed. Characterizing the axial dipole clearly requires a more sophisticated AR2 process, with a second distinct time-scale.

Key words: Dynamo: theories and simulations; Magnetic field; Rapid time variations; Probability distributions; Time-series analysis; Inverse theory.

1 INTRODUCTION

The construction of global field models or of regional master-curves from geomagnetic records has required the use of spatial and temporal regularizations (e.g., Jackson et al. 2000; Korte et al. 2009; Thébault and Gallet 2010). Searching for models as smooth as possible (e.g., Constable and Parker 1988a) allows to retrieve the features that are reliably constrained by the data, but does not give access to uncertainties on model coefficients. To address this issue, geomagnetic models have been produced using prior information in the form of covariance matrices for the model parameters. These matrices have been built using either some knowledge of the temporal variability of the present geomagnetic field, which we will further discuss here, or spatial cross-covariances deduced from geodynamo simulations (e.g., Fournier et al. 2013, 2015). Such prior information is particularly useful when modeling the Earth's magnetic field on historical and archeological time-scales, for which the data distribution is sparse in both space and time, and is characterized by large measurements (and sometimes dating) errors. Finally, prior information in the form of covariance matrices is a prerequisite for data assimilation. For instance, knowledge of the analysis covariance matrix in sequential assimilation is necessary to forecast future trajectories of the geomagnetic field (e.g., Gillet et al. 2015; Aubert 2015).

In the probabilistic framework of assimilation algorithms, geomagnetic spherical harmonic coefficients are assumed to result from Gaussian processes. These are stationary stochastic processes fully specified by their means and auto-covariance functions (MacKay 1998). As a matter of fact, the auto-covariance function of any stationary stochastic process can be deduced from its frequency spectrum. Analyses of geomagnetic records suggest that their power spectrum P behaves as $P(f) \propto f^{-s}$ in some ranges of frequency f , with s the spectral index (e.g., Constable and Johnson 2005; Panovska et al. 2013). This defines scale invariance. The index value is related to the underlying physical processes and to the statistical properties of the time-series.

Studies of the Earth dipole moment (Constable and Johnson 2005) suggest a flat energy density

54 spectrum ($s = 0$) for the longest time-scales (1 Myr or more). This spectrum steepens towards higher
 55 frequencies, with a spectral index $s \simeq 2$ at millennial to centennial time-scales (Panovska et al. 2013)
 56 and $s \simeq 4$ from centennial to inter-annual time-scales (De Santis et al. 2003). Considering the un-
 57 signed dipole moment for the past 2 Myr, Brendel et al. (2007) and Buffett et al. (2013) found that
 58 its spectrum, over millennial periods, has also a spectral index of 2, and made the analogy with spec-
 59 tra from realisations of autoregressive stochastic processes of order one (AR1). These processes have
 60 continuous but non differentiable samples. They are also known as Ornstein-Uhlenbeck processes and
 61 are solutions of a Langevin-type equation (Gardiner 1985). Buffett et al. (2013) argued that the charac-
 62 teristic time-scale of the deterministic part of the stochastic process that they constructed from dipole
 63 series is set by the dipole decay time t_d . In this framework, this time is related to the escape time for
 64 bistable systems that they also connect to the rate of magnetic reversals. Buffett (2015) also studied
 65 the relation of this time to the duration of polarity transitions.

66 Although the axial dipole field has been the focus of many studies, the non-dipolar field is much
 67 less documented. On time-scales shorter than a few centuries, order 2 autoregressive (AR2) stochastic
 68 processes, whose samples are differentiable, have been introduced to define prior information about
 69 the auto-covariance function of the Gauss coefficients when building global magnetic field models
 70 over the observatory era (Gillet et al. 2013) and regional models over archeological periods (Hel-
 71 lio et al. 2014). They are indeed consistent with a spectral index $s = 4$ at decadal periods. Gillet
 72 et al. (2013) characterized the appropriate AR2 stochastic process from the variance and the secular
 73 variation times of the spherical harmonic coefficients. They calculated these two quantities from the
 74 geomagnetic spatial power spectrum of the geomagnetic field (Loves 1974) and of its time-derivative
 75 (the secular variation) obtained from a field model of the well documented satellite era. Considering
 76 geomagnetic series as sample functions of stochastic processes with power spectrum $P(f) \propto f^{-4}$
 77 gives an explanation to the occurrence of geomagnetic jerks, which are defined as abrupt changes in
 78 the geomagnetic field second time derivative (Mandea et al. 2010).

79 Constructing field models from realisations of AR2 processes yields time series very similar to
 80 observatory series (Brown 2015). However, the hypothesis that Gauss coefficients can be described
 81 in terms of AR2 stochastic processes is not easily tested using geomagnetic observations because
 82 we lack highly accurate, dense coverage data over a long enough time window. In particular, the
 83 satellite era is too short in comparison with the decadal to centennial correlation times involved in
 84 the evolution of the geomagnetic field. For this reason, it may be helpful to investigate the statistics
 85 of individual coefficient series from numerical simulations of the geodynamo. Although calculated
 86 for dimensionless numbers far from Earth-like parameters, numerical simulations provide us with
 87 time series of Gauss coefficients that may be used to test assumptions about the statistics of the field

coefficients (Kuipers et al. 2009; Tanriverdi and Tilgner 2011; Meduri and Wicht 2016). A major issue is the rescaling of the time axis (Lhuillier et al. 2011b; Christensen et al. 2012). Buffett et al. (2014) and Buffett and Matsui (2015) have just achieved a comparison between the frequency spectrum of the dipole term obtained from a numerical simulation and the theoretical spectrum expected for a stochastic process. In both numerical and theoretical spectra, they distinguished three domains of increasing frequencies for which the spectral index is, as described above for the observed field, $s = 0$, $s = 2$ and $s = 4$. Then, they documented the transitions between the three frequency ranges, and proposed a phenomenological interpretation of the two cut-off times: they suggest that they are related to the dipole decay time t_d and to the lifetime of convective eddies in the fluid core. Attributing the different times to specific underlying mechanisms in the geodynamo models may help to compare simulations and observations and to overcome the limitations of the numerical models.

Instead of focusing our analysis on the dipole field, we apply here stochastic modeling to spherical harmonics of higher degree. We use high-resolution numerical simulations to test a simple recipe for the auto-covariance function of the geomagnetic coefficients based on instantaneous models of the field and its time variation. We find that the AR2 stochastic processes recently used as prior by Gillet et al. (2013) and Helliou et al. (2014) do provide an approximation of the temporal power spectra for individual Gauss coefficients in the numerical simulations. Based on these results, we argue that up to millennial periods the auto-covariance function of Gauss coefficients of the actual geomagnetic field can be described with only two parameters (or three for the axial dipole).

The manuscript is organized as follows. In section 2, we give an overview of stochastic processes that we consider in this study to model the time evolution of geomagnetic Gauss coefficients. In section 3, we first give the main characteristics of the three different numerical dynamo simulations analysed throughout this study, before we describe the statistics (variance, correlation time and spectra) of the generated Gauss coefficients. Next, we compare the frequency spectra of non-dipole Gauss coefficients in our dynamo simulations with spectra predicted from the assumption that they are realisations of order 2 stochastic processes with a single characteristic time-scale. Finally in section 4 we describe possible deviations from spherical symmetry, and discuss the specific behavior of the axial dipole at millennial and longer periods. Those considerations lead us to speculate about the possible mechanisms underlying the time-scales of the stochastic processes that we have considered. We finally discuss consequences for uncertainty estimates in field modeling.

2 STOCHASTIC MODELS FOR THE TIME EVOLUTION OF GAUSS COEFFICIENTS

As stated by the Wiener-Khinchin theorem (Van Kampen 2007), a stationary stochastic process x of time t can be characterized either by its power spectrum $P(f)$ or by its auto-covariance function

121 $C(\tau) = E(x(t)x(t+\tau))$, where $E(\dots)$ stands for the statistical expectation. Those two quantities are
 122 related through

$$123 \quad P(f) = \int_{-\infty}^{\infty} C(\tau)e^{-i2\pi f\tau} d\tau. \quad (1)$$

124 We make below a connection between the stochastic processes that we use in this study and the pro-
 125 cesses that have been previously employed to model the evolution of the geocentric axial dipole.

126 2.1 A three-parameter AR2 process for the axial dipole

127 Transition between power laws $P(f) \propto f^{-4}$, f^{-2} , and f^0 at respectively high, intermediate and low
 128 frequencies have been documented for the Earth magnetic field (e.g., Constable and Johnson 2005;
 129 Ziegler et al. 2011) as well as for dynamo numerical simulations (Olson et al. 2012; Davies and
 130 Constable 2014; Buffett and Matsui 2015). Based on these observations, Hellio (2015) and Buffett
 131 and Matsui (2015) introduced specific stochastic processes for modeling the time changes of the axial
 132 dipole. Their two approaches are compared below.

133 In the following, we assume that the axial dipole coefficient samples a stochastic process $x(t)$, of
 134 non-zero average $\bar{x} = E(x)$, i.e. we consider a period of constant (normal or inverse) polarity. We
 135 discuss the fluctuations $y(t) = x(t) - \bar{x}$ about this average. Hellio et al. (2014) proposed that y is a
 136 realisation of an AR2 stochastic process, namely is solution of a differential equation of the form

$$137 \quad \frac{d^2y}{dt^2} + 2\chi \frac{dy}{dt} + \omega^2 y = \zeta(t), \quad (2)$$

138 where $\zeta(t)$ is a white noise process, and the frequencies ω and χ are positive. The latter two conditions
 139 ensure that the process is stationary. For $\chi > \omega$, the frequency spectrum exhibits f^{-4} , f^{-2} and f^0
 140 dependence at respectively high, intermediate and low frequencies. It can be expressed as (e.g. Yaglom
 141 2004)

$$142 \quad P(f) = \frac{4\chi\omega^2\sigma^2}{(\omega^2 - (2\pi f)^2)^2 + (4\pi\chi f)^2}, \quad (3)$$

143 where $\sigma^2 = E(y^2)$. It is thus constrained by three quantities: the process variance σ^2 , and the param-
 144 eters χ and ω . The auto-covariance function is given by

$$145 \quad C(\tau) = \frac{\sigma^2}{2\xi} \left((\chi + \xi)e^{-(\chi - \xi)|\tau|} - (\chi - \xi)e^{-(\chi + \xi)|\tau|} \right), \quad (4)$$

146 with $\xi^2 = \chi^2 - \omega^2$. The time ω^{-1} can be obtained as the square root of the ratio between the variance
 147 of y and of its time derivative (Hellio 2015, p.50). Indeed, the auto-covariance function C is twice
 148 differentiable at $\tau = 0$, with

$$149 \quad C''(0) = \left. \frac{d^2}{d\tau^2} C(\tau) \right|_{\tau=0} = -\sigma^2\omega^2, \quad (5)$$

150 and we have also (Hulot and Le Mouél 1994):

$$151 \quad C''(0) = -E \left[\left(\frac{dy}{dt}(t) \right)^2 \right]. \quad (6)$$

152 Buffett and Matsui (2015) model instead the evolution of $x(t)$ using the stochastic equation

$$153 \quad \frac{dx}{dt} = v(x) + \sqrt{D(x)}\Gamma(t), \quad (7)$$

154 where $\Gamma(t)$ is a red noise characterized by a Laplacian auto-covariance function, $v(x)$ is a drift term
 155 describing the slow evolution of the axial dipole moment, and $D(x)$ defines the amplitude of random
 156 fluctuations. Following Buffett et al. (2013, 2014) and Buffett and Matsui (2015), the latter two terms
 157 may be approximated by $v(x) \simeq -(x - \bar{x})/\tau_s = -y/\tau_s$ and $D(x) \simeq D$, yielding a stochastic equation
 158 of the form

$$159 \quad \frac{dy}{dt} + \frac{y}{\tau_s} = \epsilon(t), \quad (8)$$

160 with $\epsilon(t) = \sqrt{D}\Gamma(t)$. Since $\epsilon(t)$ is a Laplacian correlated noise, its evolution can be modeled by an
 161 order one stochastic equation of the form (e.g., Jazwinski 2007)

$$162 \quad \frac{d\epsilon}{dt} + \frac{\epsilon}{\tau_f} = \zeta(t), \quad (9)$$

163 with $\zeta(t)$ a white noise process.

164 Combining equations (8) and (9) leads to an equation of the form

$$165 \quad \frac{d^2y}{dt^2} + \left(\frac{1}{\tau_s} + \frac{1}{\tau_f} \right) \frac{dy}{dt} + \frac{y}{\tau_s\tau_f} = \zeta(t). \quad (10)$$

166 With $2\chi = 1/\tau_s + 1/\tau_f$ and $\omega^2 = 1/(\tau_s\tau_f)$, equation (10) defines an AR2 stochastic process similar
 167 to that defined through equation (2). Adopting $\tau_f < \tau_s$, we obtain

$$\begin{cases} \tau_s = \frac{\chi + \xi}{\omega^2} \\ \tau_f = \frac{\chi - \xi}{\omega^2} \end{cases}. \quad (11)$$

168 For $\tau_f \ll \tau_s$, we deduce from (3) and (11) that the transition period between domains of the power
 169 spectrum presenting 2 and 4 (resp. 0 and 2) spectral indices is $2\pi\tau_f$ (resp. $2\pi\tau_s$).

170 Hellio (2015) and Buffett et al. (2013) are therefore using similar stochastic models for the axial
 171 dipole. Note however that the latter implicitly states the condition ξ real and $\chi \geq \omega$ – see equation
 172 (11). Equation (2) is thus more general, and allows a wider range of behaviors.

173 **2.2 A two-parameter AR2 process for non dipole coefficients**

174 For an AR2 process with $\chi = \omega$ (i. e. $\tau_f = \tau_s$), the frequency spectrum of the process defined from
 175 (2) is given by

$$P(f) = \frac{4\omega^3\sigma^2}{[\omega^2 + (2\pi f)^2]^2}. \quad (12)$$

This power spectrum is flat (spectral index $s = 0$) at low frequencies and behaves as f^{-4} for $f \gg \omega/(2\pi)$. It does not display a power law f^{-2} at intermediate frequencies. The auto-covariance function of the process is given by

$$C(\tau) = \sigma^2 (1 + \omega|\tau|) e^{-\omega|\tau|}. \quad (13)$$

This particular autoregressive process of order 2 depends only on two parameters, the variance σ^2 and the characteristic time-scale ω^{-1} . It was used by Gillet et al. (2013), Helliou et al. (2014), and Helliou (2015) to define prior information on Gauss coefficients for the computation of global archeomagnetic and geomagnetic field models.

3 METHOD FOR CHARACTERIZING THE TIME-SPECTRA OF GAUSS COEFFICIENTS

Assuming that all Gauss coefficients but the axial dipole sample stochastic Gaussian processes of auto-covariance function (13), we use numerical geodynamo simulations to discuss how to estimate the two parameters σ and ω that characterize the processes. Then, we compare the theoretical power spectrum of these processes to the actual spectrum of the Gauss coefficients in our numerical simulations.

3.1 Simulations used in the study

We rely on three dynamo numerical simulations named Step 0 (S0), Step 1 (S1), and Coupled Earth (CE). All three solve the momentum, codensity and induction equations under the Boussinesq approximation, for an electrically conducting fluid within a spherical shell of aspect ratio 0.35 between the inner core and the outer core of radius c . S0 and S1 were computed using the free XSHELLS code (Schaeffer 2015), assuming no-slip and fixed homogeneous heat flux conditions at both the inner and outer boundaries. CE (Aubert et al. 2013) was run using the PARODY-JA code (Aubert et al. 2008), assuming no-slip conditions at the inner boundary, free-slip conditions at the outer core boundary, and heterogeneous mass-anomaly flux both at the inner and at the outer boundaries. This simulation also includes a gravitational coupling between the inner core and the mantle. Both codes use finite differences in radius and spherical harmonic expansion (Schaeffer 2013), together with a semi-implicit Crank-Nicolson-Adams-Bashforth time scheme of order 2.

Non-dimensional parameters and times characterizing these simulations are given in Table 1. Dimensionless times are transformed into years following Lhuillier et al. (2011b) – see also sections 3.2 and 4.3. The field intensity is also rescaled to dimensional units using a proportionality constant such

206 that the averaged root mean square (r.m.s.) field in the shell is equal to 4 mT, a value comparable to
 207 that estimated for the Earth’s core by Gillet et al. (2010).

208 The longest simulations S0 and CE allow to investigate long time-scales, whereas the high sam-
 209 pling rate and the small Ekman number in S1 give access to shorter time-scales. All three simulations
 210 are dipole-dominated at the Core Mantle Boundary (CMB); see the relative dipole field strength f_{dip}
 211 in Table 1. They also display non-dipolar structures and significant secular variation (but no polarity
 212 reversal). The field in CE has the particularity to show prominent equatorial structures that undergo
 213 a westward drift, as observed for the Earth’s magnetic field over the past four centuries (Finlay and
 214 Jackson 2003). It is also important to notice that the magnetic Reynolds number Rm (defined as the
 215 ratio of magnetic diffusion time over advection time) in our three simulations is close to the Earth’s
 216 core value (see Table 1).

217 Statistics over periods much longer than a few 10,000 years (e.g. involving reversals) would re-
 218 quire much longer simulations. There is thus a trade-off between capturing the long term evolution
 219 of dipole moment changes and reproducing rapid field variations (Meduri and Wicht 2016). Robust
 220 estimates of the mean dipole field strength require simulations over many diffusion times that are
 221 presently achievable only for large Ekman number (e.g., Olson et al. 2012; Davies and Constable
 222 2014). Because we are particularly interested here into decadal to millennial time-scales, we use pa-
 223 rameters closer to (yet still far away from) the geophysical ones. Our simulations thus cover a wide
 224 range of periods shorter than the turn-over time t_U .

225 We show in Fig. 1 and 2 examples of the time series that we analyse in the rest of the paper.
 226 The axial dipole has a non-zero mean value and displays large long-period fluctuations. We observe a
 227 decrease of both the amplitude and the time-scale of fluctuations of the other coefficients with degree.
 228 While temporal fluctuations of all coefficients seem rather stationary in simulations S0 and CE (Fig.
 229 1), non-stationarity is observed in the shorter simulation S1 for the largest degrees (Fig. 2, right). Note
 230 that periodic oscillations are observed for coefficient \mathcal{G}_2^1 in CE. These oscillations will be discussed in
 231 section 4.2.

232 3.2 Variance and correlation time of Gauss coefficients

233 The magnetic field \mathbf{B} outside the core is described through a scalar potential V such that $\mathbf{B} = -\nabla V$.
 234 In this work, Gauss coefficients \mathcal{G}_n^m and \mathcal{H}_n^m are defined at the core surface (and not at the Earth’s
 235 surface) with n and m the spherical harmonics degree and order, N the truncation degree, hence V is
 236 decomposed as

$$237 \quad V(r, \theta, \phi, t) = c \sum_{n=1}^N \left(\frac{c}{r}\right)^{n+1} \sum_{m=0}^n (\mathcal{G}_n^m(t) \cos m\phi + \mathcal{H}_n^m(t) \sin m\phi) P_n^m(\cos \theta), \quad (14)$$

Name	Definition	S0	S1	CE	C-600	C-1400	Earth's core
Ekman	$E = \nu/(\Omega D^2)$	10^{-5}	10^{-6}	$3 \cdot 10^{-5}$	$5 \cdot 10^{-5}$	$5 \cdot 10^{-5}$	$4 \cdot 10^{-15}$
Flux Rayleigh	$Ra_F = FD^2/4\pi\rho\kappa^2\nu$	$4.4 \cdot 10^{10}$	$8.9 \cdot 10^{11}$	$1.0 \cdot 10^9$	$3.1 \cdot 10^7$	$1.5 \cdot 10^8$?
Magnetic Reynolds	$Rm = UD/\eta$	710	660	940	42	90	1700
Prandtl	$Pr = \nu/\kappa$	1	1	1	1	1	0.1 – 10
Magnetic Prandtl	$Pm = \nu/\eta$	0.4	0.2	2.5	0.5	0.5	$2 \cdot 10^{-6}$
Alfvén time	$t_A = D\sqrt{\mu_0\rho}/B$	100	47	110		83	2
Dipole decay time	$t_d = c^2/(\pi^2\eta)$	$1.2 \cdot 10^4$	$1.2 \cdot 10^4$	$3.2 \cdot 10^4$	$1.2 \cdot 10^3$	$2.7 \cdot 10^3$	$5 \cdot 10^4$
Turn-over time	$t_U = D/U$	69	76	140	120	120	120
Dissipation time [†]	τ_{diss}^{mag}	12	14.5	41			
Dipole field strength [‡]	f_{dip}	0.73	0.68	0.75			0.68
Simulation duration		$85 \cdot 10^3$	$7.6 \cdot 10^3$	$84 \cdot 10^3$		$91 \cdot 10^3$	
Sampling interval		38	0.25	5.3		11	

Table 1. Non-dimensional numbers and time-scales for numerical simulations and the Earth's core. All times are given in years. D is the shell thickness, c is the outer core radius, B and U the root mean square of the magnetic field intensity and of the velocity in the fluid shell, Ω the rotation rate, η the magnetic diffusivity, ν the kinematic viscosity, κ the thermal diffusivity, μ_0 the magnetic permeability of free space, F the mass anomaly flux at the Inner-Core boundary (chemical convection, see Aubert et al. 2013). C-600 and C-1400 stand for the Calypso simulations of Buffett and Matsui (2015), after translating their time-scale into the τ_{SV} -based scaling used throughout this paper, with $\tau_{SV} = 14t_d/Rm$ (Lhuillier et al. 2011a). See Backus et al. (1996, pp 200-204) for the calculation of the dipole decay time t_d . [†]We refer to Christensen and Tilgner (2004) for the definition of the magnetic dissipation time τ_{diss}^{mag} , ratio of magnetic energy to Ohmic dissipation. [‡]The relative dipole field strength at the core surface f_{dip} is defined as in Christensen and Aubert (2006). We have adopted $\nu = 1.5 \cdot 10^{-6} \text{ m}^2\text{s}^{-1}$, $\eta = 0.75 \text{ m}^2\text{s}^{-1}$, $\rho = 1.1 \cdot 10^4 \text{ kg}\cdot\text{m}^{-3}$, $\tau_{SV} = 415 \text{ yrs}$ and $B = 4 \cdot 10^{-3} \text{ T}$ to give values for the Earth's core. The turn-over time deduced from τ_{SV} and Lhuillier et al. (2011a), $t_U = D/U \simeq 0.3 \tau_{SV} \simeq 125 \text{ yrs}$, is consistent with $U \sim 20 \text{ km}\cdot\text{yr}^{-1}$ in the Earth's core and is within a factor of two of our estimates from simulations.

238 where r is the distance to the Earth center, θ the colatitude, ϕ the longitude, and P_n^m are the Schmidt
 239 quasi-normalized Legendre functions. We define the spatial power spectra for the geomagnetic field
 240 and its secular variation

$$\begin{cases} R_n = (n+1) \sum_{m=0}^n [E(\mathcal{G}_n^{m2}) + E(\mathcal{H}_n^{m2})] \\ S_n = (n+1) \sum_{m=0}^n [E(\partial_t \mathcal{G}_n^{m2}) + E(\partial_t \mathcal{H}_n^{m2})] \end{cases} \quad (15)$$

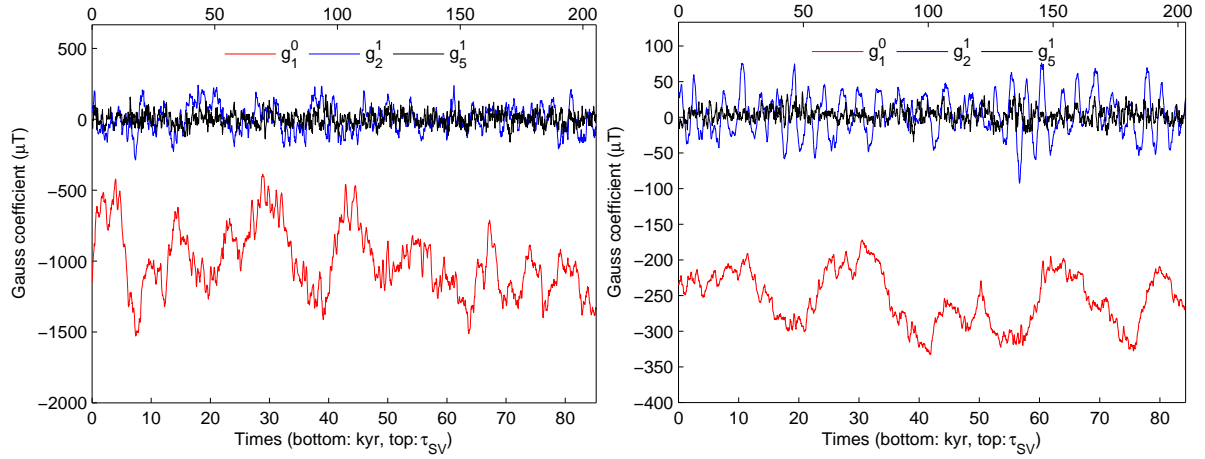


Figure 1. Time series of coefficients \mathcal{G}_1^0 , \mathcal{G}_2^1 and \mathcal{G}_5^1 from simulations S0 (left) and CE (right). The top scale gives the dimensionless time (based on τ_{SV}).

241 as functions of degree n , from which a correlation time $\tau_n = \sqrt{R_n/S_n}$ can be derived (Hulot and
 242 Le Mouél 1994).

243 The two quantities R_n and τ_n are now assumed to follow simple laws as a function of the degree
 244 n (for $n \geq 2$):

$$245 \quad R_n \simeq \alpha\beta^n, \quad \tau_n \simeq \delta n^{-\gamma} . \quad (16)$$

246 Constable and Parker (1988b) found that geomagnetic field models ($1 \leq n \leq 12$) are consistent with
 247 $\beta = 1$, whereas Roberts et al. (2003) inferred $\beta \simeq 0.90$ from observations for $n \geq 3$. Holme and
 248 Olsen (2006) and Lesur et al. (2008) examined their satellite field models and estimated $\gamma \simeq 1.45$ and
 249 $\gamma \simeq 1.375$ respectively whereas Christensen and Tilgner (2004) and Lhuillier et al. (2011b) argued

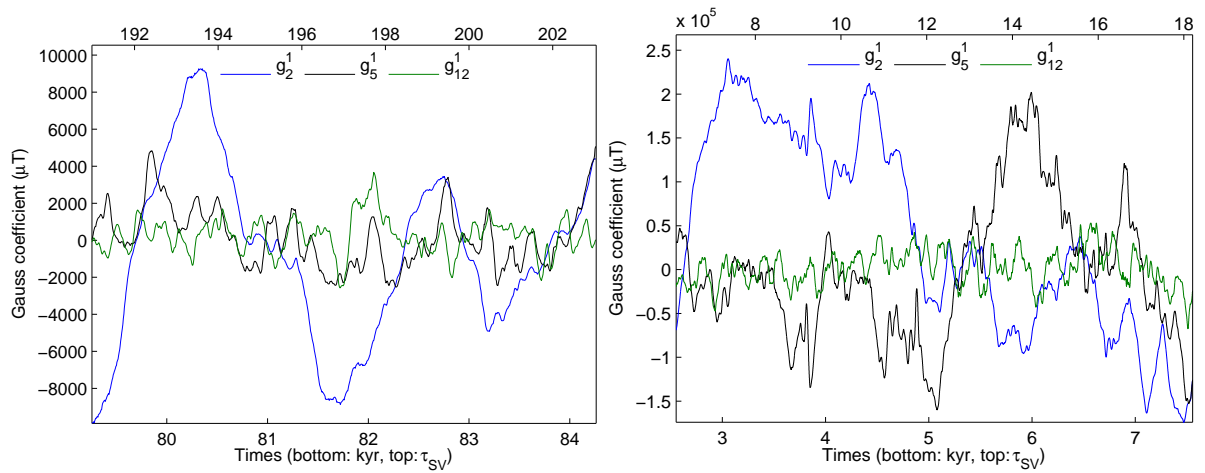


Figure 2. 5 kyr time series of coefficients \mathcal{G}_2^1 , \mathcal{G}_5^1 and \mathcal{G}_{12}^1 from simulations CE (left) and S1 (right). The top scale gives the dimensionless time (based on τ_{SV}).

250 instead for $\gamma = 1$ in joint analyses of geodynamo simulations and geomagnetic field models. The
 251 latter authors also scaled time in simulations so that $\tau_{SV} = \delta|_{\gamma=1}$ matches the geophysical value and
 252 estimated $\tau_{SV} = 415$ years from a fit of τ_n for degrees $n \in [2 - 13]$.

253 Building on these works, we shall assume $\beta = \gamma = 1$ hence a flat spatial power spectrum R_n at the
 254 CMB for the observable length-scales. This simplification allows to easily convert numerical times into
 255 years. The remaining parameters (α, δ) entering equations (16) can be derived from the average of R_n
 256 and a least-squares fit of $\log(\tau_n)$ versus $\log(n)$. Since these two quantities are not normally distributed,
 257 a more accurate estimate may be obtained using a maximum likelihood approach, as developed by
 258 Lhuillier et al. (2011b) for τ_n (see appendix A). We discuss in Appendix B the estimation of the
 259 parameters of the regression model (16) as the conditions $\beta = \gamma = 1$ are relaxed.

260 For each simulation, we have computed different estimates of the spatial power spectrum R_n and
 261 of the time τ_n : an ensemble of instantaneous values $(\hat{R}_n, \hat{\tau}_n)$ averaged over m ($0 \leq m \leq n$) only, an
 262 estimate $(\bar{R}_n, \bar{\tau}_n)$ averaged over m and the total duration of the simulations, and the similarly averaged
 263 (R_n^*, τ_n^*) once subtracted the mean values of the coefficients. Time-averaged estimates $(\bar{R}_n, \bar{\tau}_n \times n)$
 264 and $(R_n^*, \tau_n^* \times n)$ are shown in Fig. 3 for the three simulations. We also represent the fits $R_n = \alpha$
 265 and $\tau_n \times n = \delta$ calculated either with the least-square method or the maximum likelihood one.
 266 In addition, we plot two-sigma intervals for α and δ deduced from an ensemble of ten snapshots.
 267 Overall, the different time-averaged estimates of α and δ yield rather similar results given the large
 268 variability within the ensemble of snapshot estimates. Removing or not the average appears therefore
 269 as a secondary issue.

270 Spectra R_n for CE and S0 simulations are almost flat, validating the hypothesis $\beta = 1$, while that
 271 for the most extreme (lowest viscosity, strongest forcing) simulation S1 presents a slightly decreas-
 272 ing trend with n , closer to current estimates from geomagnetic field models, as further discussed in
 273 Appendix B.

274 Times τ_n reflect slightly different behaviors in all three simulations. If the hypothesis $\gamma = 1$
 275 agrees well with the outputs from CE, S1 (resp. S0) favors instead a slightly larger (resp. lower)
 276 exponent. In simulation S1, we obtain a γ value closer to 1 after removing the time-average value of
 277 the coefficients, which mainly affects τ_n estimates at low degrees. Furthermore, we note a wide time
 278 variability in the instantaneous estimates $\hat{\tau}_n$, suggesting that a snapshot estimate alone, as available
 279 from modern geophysical observations (see e.g. Holme et al. 2011) for which the long-term average
 280 of coefficients is not available, is insufficient to determine precisely γ . All in all, we conclude that the
 281 simple hypothesis $\gamma = 1$ is consistent with our three simulations (see Appendix B for more details). An
 282 error of the order of 50% may occur when measuring the magnitudes of α and δ from instantaneous
 283 values, as shown by the two-sigma interval in Fig. 3 (right) and in table A2. This translates into a

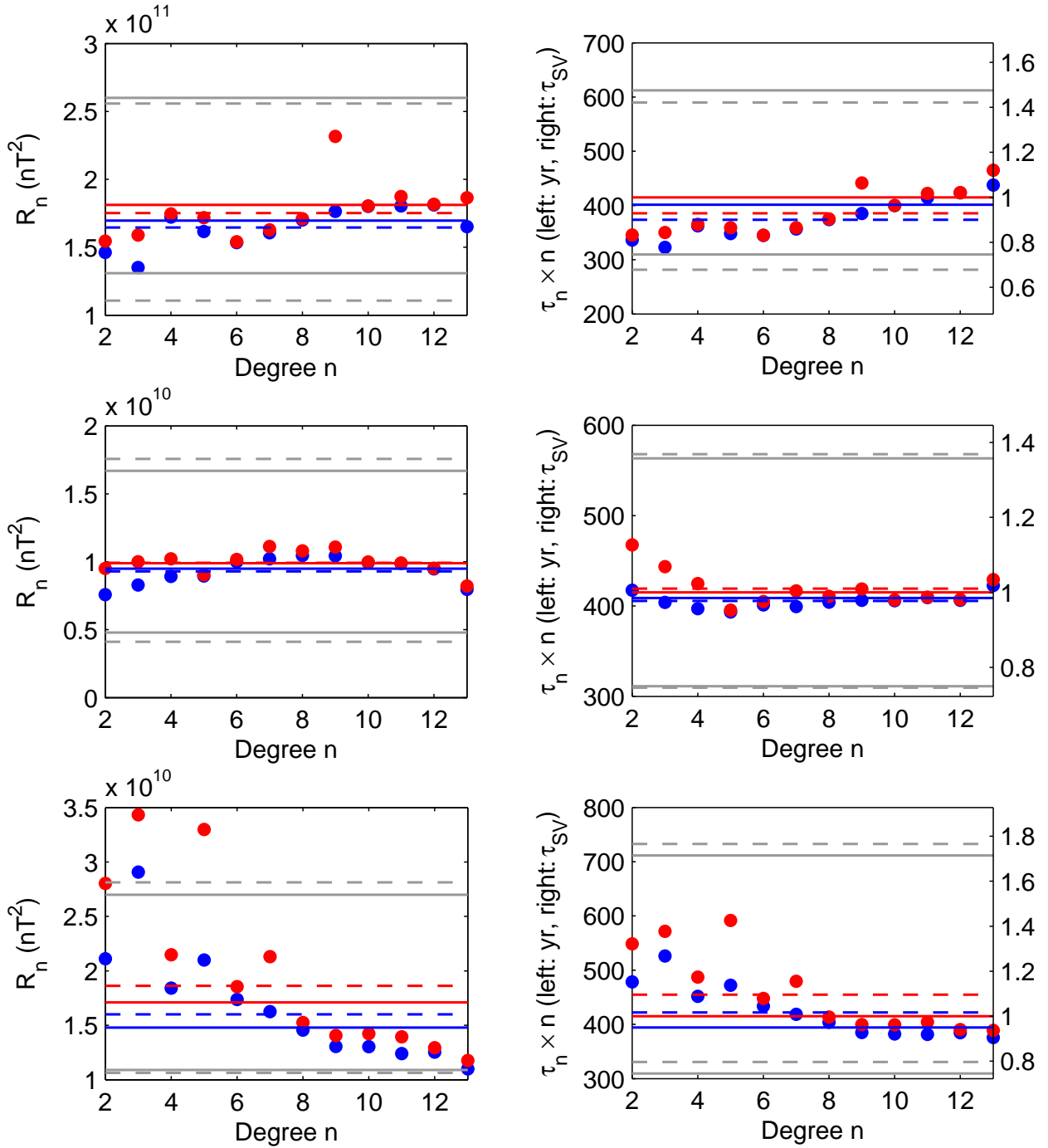


Figure 3. Spatial power spectrum R_n (left) and $n \times \tau_n$ (right) as a function of the spherical harmonic degree n for simulations S0 (top), CE (middle) and S1 (bottom) from the expected variances as in equation (15), either removing (blue dots) or keeping (red dots) the time-average of the coefficients. Dashed (resp. solid) colored lines stand for estimates of α and δ using least-squares (resp. maximum likelihood) regressions (16) with $\beta = \gamma = 1$. Grey lines represent the two-sigma intervals around the average of 10 estimates of α and δ from independent snapshots \hat{R}_n and $\hat{\tau}_n$, which are not represented. The right scale on the $n \times \tau_n$ plots gives the dimensionless time in τ_{SV} units.

284 variability in τ_{SV} significantly larger than that observed by Lhuillier et al. (2011b) from a dynamo
 285 simulation at larger viscosity and lower forcing.

286 Note that the time-series of non-dipole coefficients represented on Fig. 2 appear uncorrelated when
 287 sampled over periods longer than $2\pi\tau_n = 2\pi\tau_{SV}/n$ (i.e. for periods longer than about 1300 yr, 500
 288 yr, and 200 yr for degrees 2, 5, and 12 respectively). This suggests a flat power spectrum at lower
 289 frequencies, as expected for the two-parameter AR2 processes described in section 2.2

290 3.3 Frequency spectra of Gauss coefficients

291 In order to avoid frequency leakage when estimating the power spectrum for the finite-length time-
 292 series of Gauss coefficients, we adopt a multi taper approach (e.g., Percival and Walden 1993). The
 293 advantage of this approach is that the power spectrum variance is reduced by averaging independent
 294 estimates of the power spectrum obtained after multiplying the series by various orthogonal tapers.
 295 Several variants of the multi taper approach have been used before to assess the power spectrum of
 296 the dipole moment. Constable and Johnson (2005) relied on sine tapers (Riedel and Sidorenko 1995).
 297 Olson et al. (2012) chose instead to break the series into overlapping segments tapered using a Hanning
 298 window (Welch 1967). As Buffett and Matsui (2015), we adopt in this study an approach based on
 299 Slepian functions (Thomson 1982). We use seven Slepian tapers characterized by a power spectrum
 300 with energy concentrated in a bandwidth $[-W, W]$, where $W = 4/(N\Delta t)$, N is the number of data,
 301 and Δt is the sampling interval. As a consequence, the power spectrum estimated at a given frequency
 302 f is controlled by values of the power spectrum within $[f - W, f + W]$, with W the resolution of the
 303 power spectrum.

304 We test the multi taper approach of Thomson (1982) on a realisation of a stochastic process.
 305 The obtained spectra are further smoothed by running averages over a length that linearly increases
 306 with the frequency (from 1 point at minimum frequency to 201 points at maximum frequency). We
 307 show the spectra obtained for this realisation both before and after removing its averaged value (Fig.
 308 4). Although these power spectra include a certain amount of noise, they reproduce well both the
 309 amplitude and the spectral indices of the true power spectrum, except at frequencies lower than the
 310 resolution W . At frequencies $f < W$, the average value of the series influences the power spectra,
 311 which strongly differ whether the average is removed or not: the spectrum obtained without removing
 312 the average shows a step at low frequencies, which is an artefact. The above method for calculating
 313 spectra is used below for all our results. Note that we do not remove linear trends in the time-series
 314 before computing the spectra. Nevertheless, we checked that the shape of the spectra computed here
 315 with the multi taper approach is not significantly different whether the trend has been removed or not.

316 Fig. 5 displays power spectra for degree 5 Gauss coefficient time series at the CMB, from the three

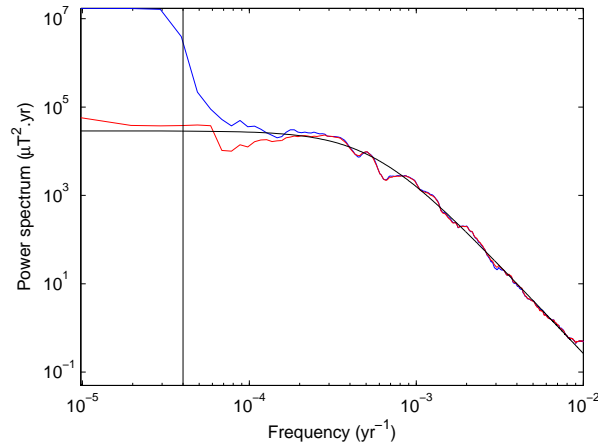


Figure 4. Comparison of power spectra for random time-series, estimated using the multi taper approach applied before (blue) and after (red) removing the averaged value of the series, and superimposed on the theoretical power spectrum (black). The series parameters are chosen to mimic a plausible behavior for the axial dipole coefficient (at the Earth’s surface): it is a Gaussian random series with an averaged value of $-35 \mu\text{T}$, a standard deviation of $5 \mu\text{T}$, with a two-parameters AR2 auto-covariance function as defined in equation (13), with $\omega^{-1} = 500$ yrs. The theoretical power spectra of this series is given in equation (12). The series contains $N = 2000$ data sampled every $\Delta t = 50$ years. The vertical black line indicates the value of the concentration half-bandwidth $W = 4/(N\Delta t)$ of the Slepian tapers. These spectra were obtained using the subroutine `pmtm` from Matlab[®] and then further smoothed using running averages.

317 simulations. For the two longest simulations (S0 and CE), we observe that spectra for all coefficients
 318 are flat (or white) at low frequencies, and show a constant spectral index at high frequencies, hinting
 319 to a scale invariance. The change of spectral index occurs within a narrow band of frequencies, and
 320 the cut-off frequency between the two regions of the spectra increases with the spherical harmonic
 321 degree, as illustrated in Fig. 6 for the CE dynamo. Whereas the spectral index at large frequencies
 322 appears independent of the spherical harmonic order in S0, it significantly increases with m in the CE
 323 and S1 simulations. Power spectra obtained from S1 do not show a flat plateau at low frequencies as
 324 a consequence of the short duration of the simulation: we do not have access to long enough periods
 325 to reach the domain where $P \propto f^0$. Spectra for this simulation show a steep decrease with f at high
 326 frequency, which is absent in the S0 and CE spectra.

327 **3.4 Comparison with the spectrum of a two-parameter AR2 process**

328 Expression (13) corresponds to a particular autoregressive process of order 2 that only depends on two
 329 parameters, a variance σ^2 and a characteristic time-scale ω^{-1} . As in Gillet et al. (2013), we further
 330 assume that these two parameters only depend on the spherical harmonic degree n , which amounts
 331 to posit that the statistics of the field are independent of longitude and latitude (Hulot and Bouligand

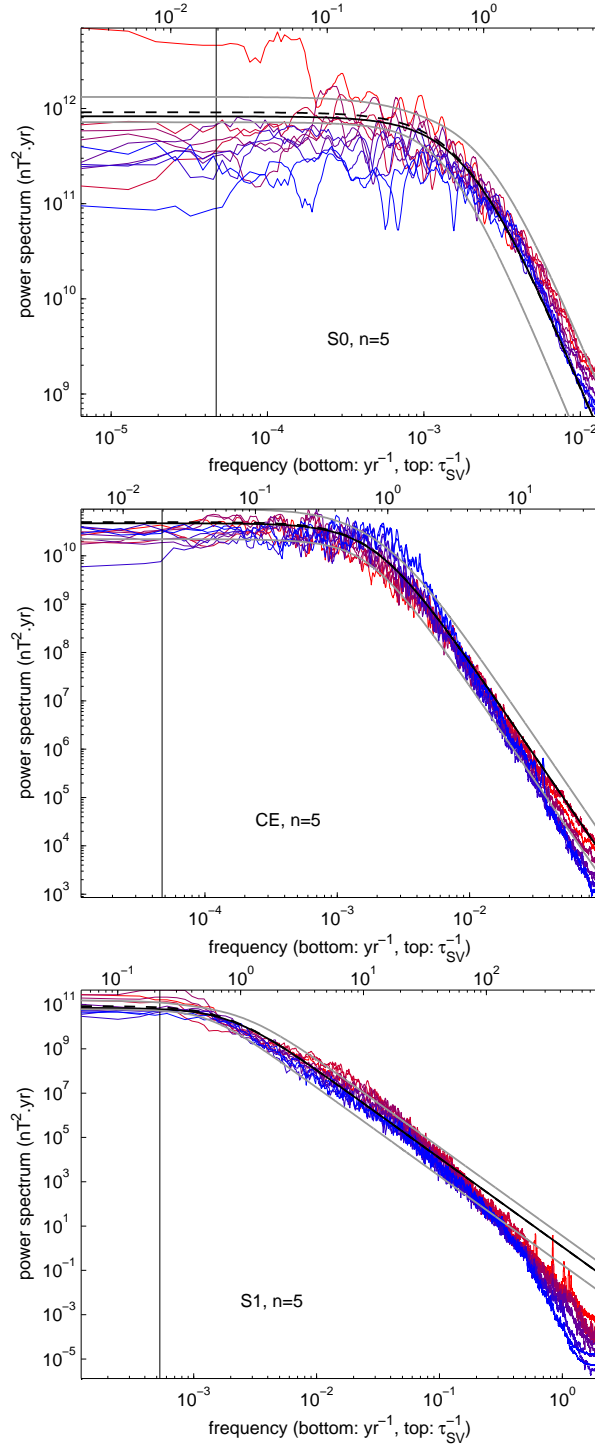


Figure 5. Power spectra computed using the multi taper approach of Thomson (1982) for coefficients of degree $n = 5$, from simulations S0 (top), CE (middle), and S1 (bottom). All coefficients \mathcal{G}_n^m and \mathcal{H}_n^m of order $m \in [0, n]$ are represented with gradually varying colors (from red for $m = 0$ to blue for $m = n$). The black solid (dashed) curves display the power spectra (12) with parameters τ_n and σ_n estimated using the maximum likelihood method and using time averaged Gauss coefficients variances in (15), once removed (or not) their averaged value. The grey lines represent the two-sigma interval around the average of 10 power spectra with parameters ω_n^{-1} and σ_n deduced from independent snapshot \hat{R}_n and $\hat{\tau}_n$. The thin vertical black line indicates the resolution half-bandwidth. The top scale gives the dimensionless frequency (based on τ_{SV}^{-1}).

2005). Then, for each degree n , one deduces from (15) that $\sigma_n^2 = R_n/(n+1)(2n+1)$, and from equations (5) and (6) the relation $\omega_n^{-1} = \tau_n$; these two parameters define the auto-covariance functions $C_n(\tau)$.

Since long enough geophysical series to produce statistical averages are not available, Gillet et al. (2013) approximated (R_n, τ_n) by the quantity $(\hat{R}_n, \hat{\tau}_n)$ estimated from a snapshot of the well documented (and supposedly representative) satellite era. This approximation relies on the assumption that main field and secular variation series are unbiased, i.e. $E(\mathcal{G}_n^m) = E(\mathcal{H}_n^m) = E(\partial_t \mathcal{G}_n^m) = E(\partial_t \mathcal{H}_n^m) = 0$. This assumption is certainly not valid for the axial dipole between two polarity reversals. For this reason, Helliou et al. (2014) considered instead dipole deviations in the expression (15) for $n = 1$. We test here the validity of using snapshot estimate $(\hat{R}_n, \hat{\tau}_n)$ to define the auto-covariance function of non-dipole coefficients.

For each simulation, we estimate parameters α and δ entering (16) (with $\beta = \gamma = 1$) using both averaged and instantaneous estimates of the spatial power spectrum and correlation times (i.e., $(\bar{R}_n, \bar{\tau}_n)$, (R_n^*, τ_n^*) and $(\hat{R}_n, \hat{\tau}_n)$) and a maximum likelihood approach. α and δ are then used to determine variances σ_n^2 and correlation times ω_n^{-1} , and to predict the theoretical spectrum (12) for all degrees n . We then estimate a two-sigma interval from 10 spectra (12) deduced from snapshots. These curves are superimposed in Fig. 5 (for $n = 5$) and Fig. 6 (CE simulation for $n = 2, 5, 12$) on spectra of the Gauss coefficients.

For all three simulations and all degrees, we observe overall a good agreement between the different theoretical spectra, with some discrepancies that we detail in the next paragraph. The theoretical spectra obtained from averaged estimates once removed or not the coefficient averaged value are very close, suggesting that the assumption of unbiased series is valid. The two-sigma intervals are relatively narrow compared to the noise level in the individual spectra and to the variability among spectra of same degree, showing that the use of snapshot estimates is appropriate.

For simulation S0, the power-spectra calculated from (12) reproduce very well the power spectra of the field coefficients at all frequencies. For simulation CE, the spectrum (12) approximates relatively well the power spectra of low order Gauss coefficients for all degrees n . On the other hand, the power spectra for the largest order coefficients ($m \sim n$) decreases more rapidly than f^{-4} at its high frequency end. Simulation S1 also presents, at periods shorter than 10 years, Gauss coefficient power spectra steeper than f^{-4} . Buffett and Matsui (2015) conjecture that the occurrence of a period range presenting a $s = 6$ spectral index, as observed from numerical computations (Olson et al. 2012; Davies and Constable 2014), could be related with a mechanism involving magnetic diffusion below the CMB. However, the identification of a spectral index s requires a power-law behavior $P(f) \propto f^{-s}$ over a significant frequency range. Instead, a power spectrum $P(f) \propto \exp(-f)$, which is reminiscent of a

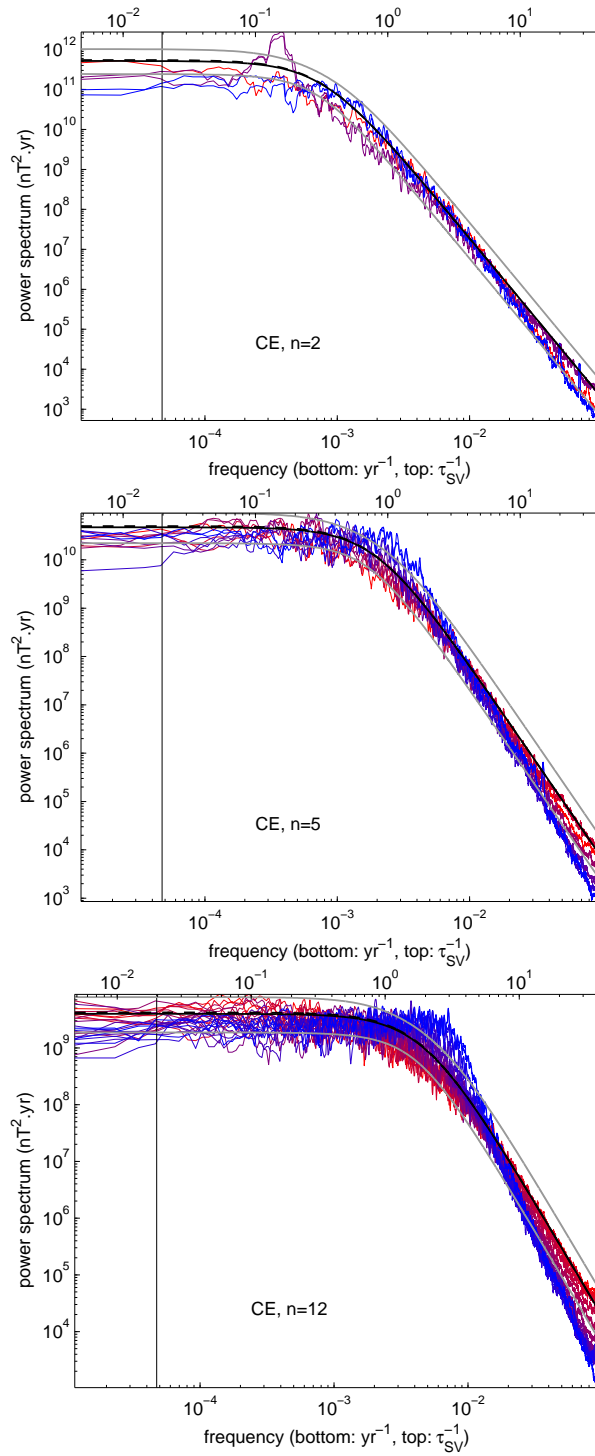


Figure 6. Power spectra for Gauss coefficients series of spherical harmonic degrees 2, 5 and 12, from the CE simulation. Same colors and line types as in Fig. 5.

366 dissipation range (see e.g. Frisch 1995), may arguably be observed at high frequencies in simulation
 367 S1. Hence, the narrow range of frequencies that displays a spectral index of 4 may result from too
 368 important diffusive processes in simulations (see §4.3).

369 4 DISCUSSION

370 4.1 Model for dipole fluctuations

371 The minimal model (12), which appears appropriate for all Gauss coefficients but the axial dipole in
 372 our simulations, involves only one time-scale ω^{-1} . It can be presented (see §2.1) as a special case
 373 ($\omega = \chi$, *i.e.* $\tau_s = \tau_f$) within a more general family of models (3) having two distinct time-scales ω^{-1}
 374 and χ^{-1} – or equivalently τ_s and τ_f , see equation (11). For $\omega < \chi$, the associated power spectra (3)
 375 show a power law in f^{-2} at intermediate frequencies – between frequencies $1/(2\pi\tau_s)$ and $1/(2\pi\tau_f)$.
 376 For this reason, they were employed by Buffett and Matsui (2015) to account for the spectrum of the
 377 axial dipole as inferred from numerical simulations and from geomagnetic models. We concur with
 378 these results. In the two simulations S0 and CE that are long enough to address long-lived dipole
 379 fluctuations, the power spectrum for the axial dipole coefficient \mathcal{G}_1^0 does not present a sharp transition
 380 from 0 to 4 spectral index (see Fig. 7). Contrary to the equatorial dipole coefficients \mathcal{G}_1^1 and \mathcal{H}_1^1 ,
 381 whose spectra are well fitted by a two parameters AR2 spectrum (12), the spectrum for \mathcal{G}_1^0 shows an
 382 intermediate spectral index over about one decade, which is well fitted by the three parameter function
 383 (3).

384 The calculation of τ_s and τ_f by Buffett and Matsui hinges on the determination of the two transi-
 385 tion frequencies between domains of spectral index 4, 2, and 0 respectively (see §2.1). Fig. 7 illustrates
 386 our fit between the spectra for S0 and CE and the function (3) where we have entered our estimations
 387 for ω and χ (directly related to τ_s and τ_f). Table 2 gives a comparison between our results and the
 388 values of τ_s and τ_f calculated by Buffett and Matsui but scaled in units of τ_{SV} . In S0 and CE, the
 389 transition frequency between domains of spectral index $s \simeq 2$ and $s \simeq 4$ (Fig. 7) leads to $\tau_f \simeq 65$
 390 and 125 yrs respectively, values about 2 to 3 times larger than the estimates by Buffett and Matsui.
 391 Switching to long periods, they made the analogy between the times τ_s and t_d found in their simula-
 392 tions. Although this analogy cannot be ruled out by our results, simulations S0 and CE show values of
 393 the ratio t_d/τ_s significantly different from 1 (see Tables 1 and 2).

394 Unfortunately, the frequency range with a flat power spectrum is clear neither in the simulations
 395 investigated here, nor in those of Buffett and Matsui. In both studies, this part of the power spectrum
 396 is within the concentration bandwidth of the taper (see their Fig. 4 and our Fig. 7); we thus cannot
 397 determine if this is to be associated with a real feature of the axial dipole power spectrum, or with

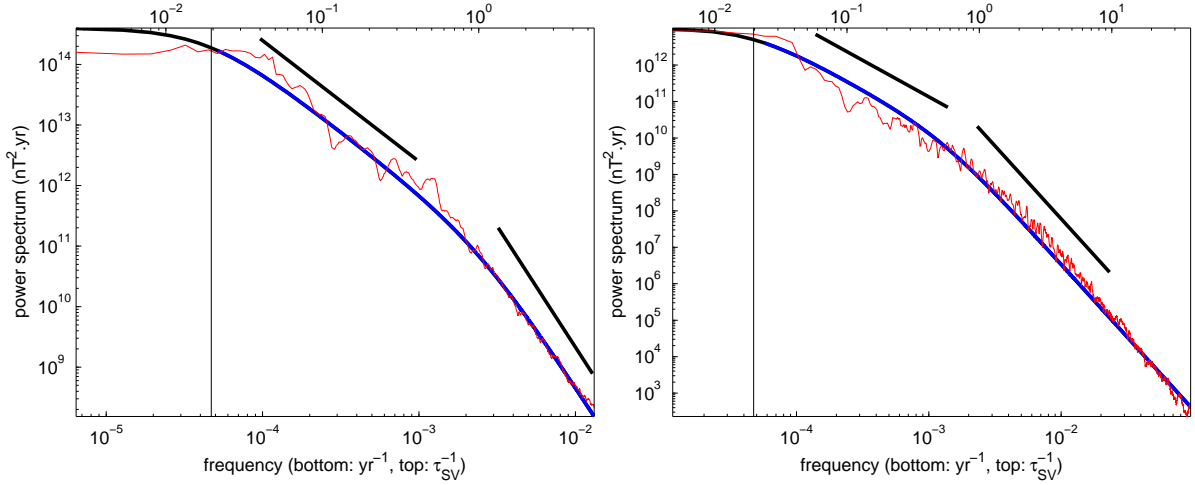


Figure 7. Power spectra (red) for the axial dipole series from simulations S0 (left), and CE (right). In black are superimposed the three parameters AR2 spectra (3) fitted to the series spectra for $f > W$ – range covered by the blue fit. The parameter W denotes the resolution half-bandwidth. The axial dipole variance is obtained directly from the series (removing the average). The frequency ω is estimated from the square root of the ratio of the variances of \mathcal{G}_1^0 and $\partial\mathcal{G}_1^0/\partial t$. The remaining parameter χ is obtained by minimizing the L2 norm of the difference between the logarithms of \mathcal{G}_1^0 series spectrum and of (3). The top scale gives the dimensionless frequency (based on τ_{SV}^{-1}). The thin vertical line indicates $f = W$. Black segments indicate spectral indices of 2 and 4.

398 an artefact due to tapering. As a result, the estimates of τ_s obtained from numerical simulations and
 399 given in Table 2 are not very accurate. Nevertheless, all estimates for $\omega^{-1} = (\tau_s \tau_f)^{1/2}$ obtained from
 400 numerical series of the axial dipole are within a factor of 2 of the value that we would obtain by
 401 extrapolating the relation $\omega_n^{-1} = \tau_n = \tau_{SV}/n$ (used for non-dipole coefficients) to the degree $n = 1$
 402 (i.e., $\omega^{-1} = 415$ yr).

403 The time ω^{-1} inferred from paleo- and archeomagnetic models appears significantly longer than
 404 estimates deduced from numerical simulations. In our opinion, the spectra of archeomagnetic field
 405 models, in the high frequency range where the spectral index is $s \simeq 4$, are much influenced by the
 406 regularization used in their construction. This explains why these models do not resolve geomagnetic
 407 jerks.

408 4.2 Deviations from spherical symmetry

409 Whereas temporal spectra from simulation S0 are fairly independent of the order m for all degrees
 410 but $n = 1$ (Fig. 5), suggesting that fluctuations of the non-dipole field are spherically symmetric at
 411 the CMB, we detect some significant dependence on the order from computations CE and S1. In CE,
 412 the spectra for coefficients of large order ($m \simeq n$) present a larger spectral index at high frequencies.

Model/Simulation	τ_s (yr)	τ_f (yr)	ω^{-1} (yr)	Reference
PADM2M ^{†1} - CALS10k.1b ^{†2}	29 000	100-200	1700-2400	Buffett et al. (2013); Buffett and Matsui (2015)
Calypso (Rm=90)	1050	37	200	Buffett et al. (2014); Buffett and Matsui (2015)
Calypso (Rm=42)	1100	35	200	Buffett and Matsui (2015)
S0	3610	65	480	
CE	3490	125	660	

Table 2. Time-scales τ_s and τ_f involved to reproduce the power spectrum of the axial dipole deduced from archeo- and paleo-magnetic observations and from dynamo numerical simulations (see the definitions of τ_s and τ_f in equations (8) and (9) respectively). The time ω^{-1} is obtained as $(\tau_s\tau_f)^{1/2}$. The different times of the Calypso simulations have been converted into the τ_{SV} -based scaling adopted throughout the paper, using $t_d = Rm \times \tau_{SV}/14$ (Lhuillier et al. 2011a). ^{†1} Ziegler et al. (2011), ^{†2} Korte and Constable (2011).

413 As a consequence, more energy is contained in coefficients of small order at high frequencies and in
414 coefficients of large order at intermediate frequencies (for periods typically from 100 to 1000 yrs).
415 Because spherical harmonics of low and large orders have their largest contributions at respectively
416 high and low latitudes, this suggests fluctuations at intermediate periods are stronger at low latitude
417 (equatorial features primarily project into sectorial coefficients). This likely reflects the westward drift
418 of low latitude structures observed in the CE simulation (see Aubert et al. 2013).

419 The power spectra for coefficients \mathcal{G}_2^1 and \mathcal{H}_2^1 in simulation CE (and to a lesser extent for order
420 1, degrees 4 and 6 coefficients, not shown) display a significant peak at periods around 2500 yrs (see
421 Fig. 6), which translates into quasi-periodic oscillations in the time-series (see Fig. 1, right). This
422 particular period corresponds to the time needed to circumnavigate the outer core at the average speed
423 of the westward drift (Aubert et al. 2013). These periodic variations mainly affect $m = 1$ coefficients
424 of the magnetic field through the advection of the eccentric gyre resulting, in the CE scenario, from
425 the heterogeneous heat fluxes.

426 The topology of field patches at the CMB is influenced by the underlying dynamics. Indeed, the
427 predominant Coriolis force in geodynamo simulations favors columnar structures aligned with the
428 rotation axis, and together with magnetic forces it textures the vorticity field in the equatorial plane
429 (e.g. Kageyama et al. 2008). As a result of field concentration by the vortices, the magnetic field at the
430 CMB (outside the polar caps above and below the inner core) shows thin filaments primarily aligned
431 along meridians (e.g. Takahashi and Shimizu 2012). This is illustrated in Fig. 8 for our lowest viscosity
432 case, the strongly forced computation S1. We have thus some evidence that the Gauss coefficients at
433 the core surface cannot be treated as independent variables.

434 We deduce the following consequences for the inversion of geomagnetic data. First, using an
435 AR2 autocorrelation function that is independent of the coefficient order as prior information for the

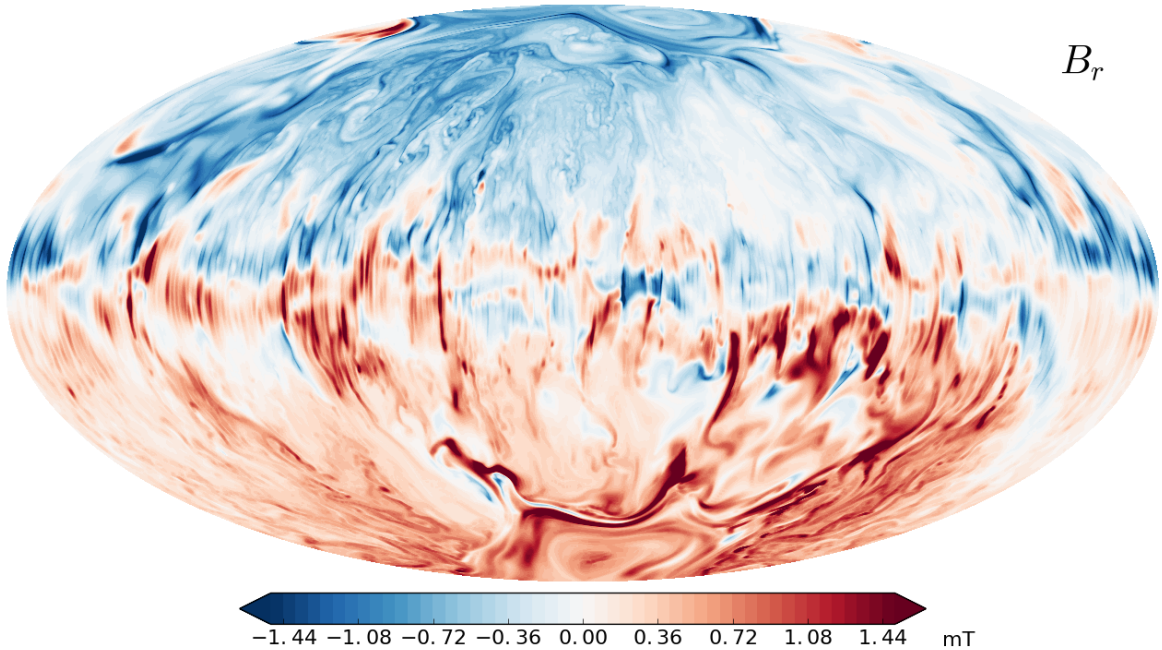


Figure 8. Full resolution snapshot of the radial magnetic field at the CMB for the S1 simulation, shown using an Aitoff projection. In this snapshot, the maximum intensity of the magnetic field at the CMB is about 7 mT.

436 inversion of geomagnetic models may penalize actual features of the geomagnetic field such as the
 437 westward drift of equatorial flux patches (Finlay and Jackson 2003) or periodic signals. Second, ac-
 438 counting for spatial cross-covariances (as performed with twin experiments on geodynamo simulations
 439 by Fournier et al. 2013) may improve the construction of prior information in field modeling studies.

440 4.3 Mechanisms underlying the different time-scales

441 Our approximation for the spectra of all coefficients but the axial dipole involves only one time-
 442 scale ω_n^{-1} ($= \tau_{SV}/n$). Lhuillier et al. (2011a) argued that τ_{SV} is related to the advection time t_U ,
 443 $\tau_{SV} \simeq 3t_U \simeq 14t_d/Rm$ (see table 1 for definitions) and this relationship holds within a factor of 2
 444 in our simulations. This link between τ_{SV} and t_U suggests that the advection time, or eddy turnover
 445 time, controls the times ω_n^{-1} .

446 Our observation, from simulations S0 and CE, of a sharp transition between 0 and 4 spectral
 447 index ranges suggests that fluctuations of non-dipole coefficients are controlled by a single time-scale,
 448 or by two time-scales that are not significantly different. In our simulations, the axial dipole is the
 449 only coefficient for which we found necessary to consider AR2 processes defined with two distinct
 450 time-scales in order to account for the existence of a frequency range displaying a spectral index
 451 of 2. One could wonder as Buffett et al. (2013) whether this is to be related to the specificity of
 452 the axial dipole to show a non-zero average value. However, in this regard, our simulations may not

453 be representative of the Earth magnetic field. Indeed, differences between time-scales are smaller in
 454 simulations than they are for the Earth’s core (see Table 1). In particular the ratio between the Alfvén
 455 time and the vortex turn-over time is about unity in simulations, instead of 10^{-2} in the Earth’s core,
 456 which potentially shrinks the dynamics at periods between a few years and a few centuries in numerical
 457 computations. Therefore, if two time-scales were involved in the fluctuations of the Earth non dipole
 458 coefficients, these time-scales may be too close in simulations to be clearly distinguished. Relatively
 459 larger magnetic energy (and thus shorter Alfvén time) can be achieved in computations at Pm larger
 460 than unity (see e.g. Dormy 2016). Such computations unfortunately tend, at low Ekman numbers, to
 461 produce dynamos with Rm significantly lower than that of the Earth.

462 The simulation S1 covers a higher frequency range than S0 and CE. In this simulation, we observe
 463 that the spectrum becomes steeper than f^{-4} at periods shorter than a cutoff period $2\pi\tau \sim 3$ years (see
 464 Fig. 5 bottom). From the inspection of other spectra ($n \neq 5$, not shown), we find no evidence of
 465 the dependence of this cut-off time on the degree. Olson et al. (2012) also suggested, from dynamo
 466 simulations, a transition at high frequency towards a f^{-6} dependence in the axial dipole spectrum.
 467 They attributed this transition to the damping effect of the viscous layer beneath the outer boundary.
 468 Following these authors and interpreting the time τ as a magnetic dissipation time through a surface
 469 layer of thickness ϵ , i.e. $\tau = \epsilon^2/\eta = \pi^2 t_d \epsilon^2/c^2$, we find $\epsilon \sim 2 \cdot 10^{-3}c$. As a result, the thickness
 470 of the dissipative layer ϵ is found to be about three times the Ekman layer thickness, $E^{1/2}D$ (e.g.,
 471 Greenspan 1968). Simulations differ from the geophysical situation inasmuch they are controlled by
 472 viscosity (King and Buffett 2013; Soderlund et al. 2012; Cheng and Aurnou 2016), with length-scales
 473 for viscous and magnetic dissipation being comparable. In a more Earth-like regime where viscosity
 474 is negligible, we can expect a dissipation cutoff at higher frequency associated to a thinner dissipative
 475 layer. We have indeed no evidence of a cut-off period from geomagnetic observations (Finlay et al.
 476 2013).

477 **4.4 Concluding remarks**

478 The two sketches presented in Fig. 9 summarize our interpretation of the coefficients power spectra,
 479 relating the cut-off periods between domains with different spectral indices to several characteristic
 480 time-scales.

481 The analysis of our simulations indicates that the spectra of simple two-parameters AR2 processes,
 482 calibrated by instantaneous values of R_n and τ_n , provide a good approximation of the spectra of all
 483 individual Gauss coefficients but the axial dipole. Although the axial dipole requires a more sophisti-
 484 cated AR2 process to account for the spectral index of 2 observed at millennial and longer periods, the
 485 use of a two-parameters process may still be sufficient for the construction of geomagnetic models.

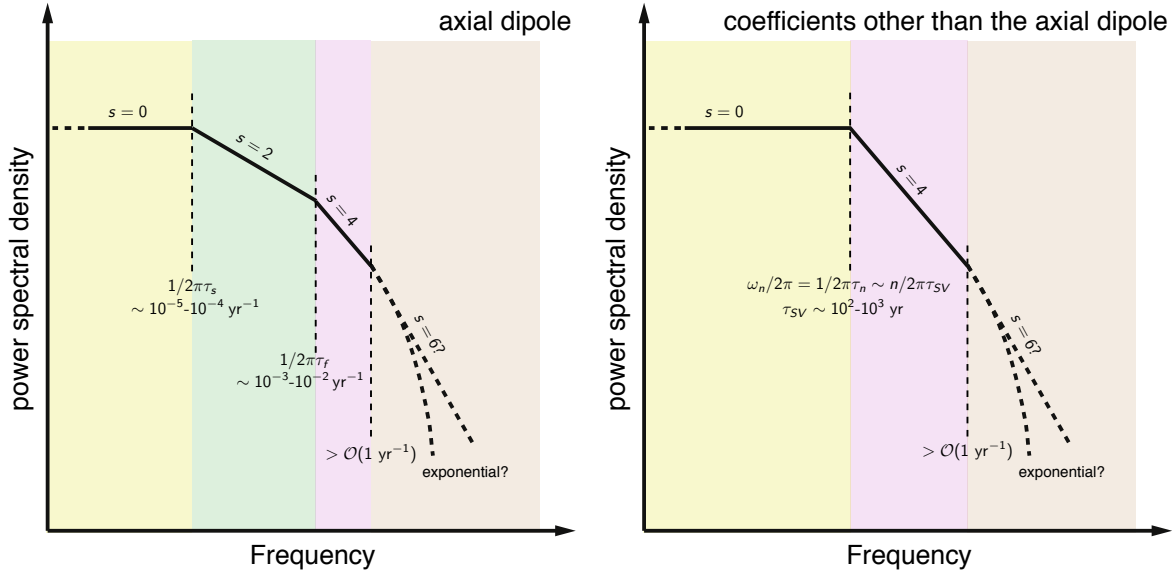


Figure 9. Schematic view of the power spectrum for the axial dipole (left) and non-dipole (right) coefficients. We associate the cut-off frequencies between domains of different spectral indices to several typical time-scales. Note that there is a factor of 2π between the cut-off periods in the power spectra and the time-scales τ_s and τ_f of equation (11).

486 Indeed, prior information is mainly needed to quantify the high frequency variability of the coeffi-
 487 cients (Hellio et al. 2014). In particular, the axial dipole being well constrained by measurements, the
 488 behavior of its prior at low frequency does not matter much.

489 Previous to this work, it was already known that there is a good agreement for the spectrum of
 490 the axial dipole between simulations and observations (Buffett and Matsui 2015). Assuming that this
 491 correspondence holds for the other field coefficients, we end up with a prescription for the prior needed
 492 to model the observed field, namely the covariance function (13) in the non-dipolar case.

493 5 ACKNOWLEDGMENTS

494 This work was motivated and initiated during Gabrielle Hellio’s PhD thesis whose purpose was to build
 495 new Bayesian models of the archeomagnetic field incorporating realistic a priori covariances describ-
 496 ing the temporal behavior of Gauss coefficients. We thank anonymous referees for their comments that
 497 helped improve the organisation and clarity of our manuscript. This work was supported by the French
 498 Agence Nationale de la Recherche under the grant ANR-2011-BS56-011 (ANR AVSGEOMAG). The
 499 XSHELLS code is freely available at <https://bitbucket.org/nschaeff/xshells>. Nu-
 500 merical simulations were run on HPC resources from PRACE and GENCI at Curie/TGCC (Grants
 501 2010PA1039, 2010PA1413, t2014047258), on the S-CAPAD platform (IPGP, France) and on the

502 Froggy platform of the CIMENT infrastructure (<https://ciment.ujf-grenoble.fr>), sup-
503 ported by the Rhône-Alpes region (GRANT CPER07_13 CIRA), the OSUG@2020 Labex (reference
504 ANR10 LABX56) and the Equip@Meso project (reference ANR-10-EQPX-29-01). ISTerre is part of
505 Labex OSUG@2020 (ANR10 LABX56). This is IPGP contribution xxxx.

506 REFERENCES

- 507 Aubert, J., 2015. Geomagnetic forecasts driven by thermal wind dynamics in the Earth's core. *Geophys. J. Int.*
508 203, 1738–1751.
- 509 Aubert, J., Aurnou, J., Wicht, J., 2008. The magnetic structure of convection-driven numerical dynamos.
510 *Geophys. J. Int.* 172, 945–956.
- 511 Aubert, J., Finlay, C.C., Fournier, A., 2013. Bottom-up control of geomagnetic secular variation by the Earth's
512 inner core. *Nature* 502, 219–223.
- 513 Backus, G., Parker, R., Constable, C., 1996. *Foundations of geomagnetism*. Cambridge University Press,
514 Cambridge (UK).
- 515 Brendel, K., Kuipers, J., Barkema, G., Hoyng, P., 2007. An analysis of the fluctuations of the geomagnetic
516 dipole. *Phys. Earth planet. Int.* 162, 249–255.
- 517 Brown, W.J., 2015. Observations and characterisation of rapid variations in the Earth's internal magnetic field.
518 Ph.D. thesis. University of Leeds.
- 519 Buffett, B., 2015. Dipole fluctuations and the duration of geomagnetic polarity transitions. *Geophys. Res.*
520 *Lett.* 42, 7444–7451.
- 521 Buffett, B., Matsui, H., 2015. A power spectrum for the geomagnetic dipole moment. *Earth planet. Sci. Lett.*
522 411, 20–26.
- 523 Buffett, B.A., King, E.M., Matsui, H., 2014. A physical interpretation of stochastic models for fluctuations in
524 the Earth's dipole field. *Geophys. J. Int.* 198, 597–608.
- 525 Buffett, B.A., Ziegler, L., Constable, C.G., 2013. A stochastic model for palaeomagnetic field variations.
526 *Geophys. J. Int.* 195, 86–97.
- 527 Cheng, J., Aurnou, J., 2016. Tests of diffusion-free scaling behaviors in numerical dynamo datasets. *Earth*
528 *planet. Sci. Lett.* 436, 121–129.
- 529 Christensen, U.R., Aubert, J., 2006. Scaling properties of convection-driven dynamos in rotating spherical
530 shells and application to planetary magnetic fields. *Geophys. J. Int.* 166, 97–114.
- 531 Christensen, U.R., Tilgner, A., 2004. Power requirements of the geodynamo from ohmic losses in numerical
532 and laboratory dynamos. *Nature* 429, 169–171.
- 533 Christensen, U.R., Wardinski, I., Lesur, V., 2012. Timescales of geomagnetic secular acceleration in satellite
534 field models and geodynamo models. *Geophys. J. Int.* 190, 243–254.
- 535 Constable, C., Johnson, C., 2005. A paleomagnetic power spectrum. *Phys. Earth Planet. Int.* 153, 61–73.

- 536 Constable, C., Parker, R., 1988a. Smoothing, splines and smoothing splines; their application in geomag-
537 netism. *J. Comput. Phys.* 78, 493–508.
- 538 Constable, C.G., Parker, R.L., 1988b. Statistics of the geomagnetic secular variation for the past 5 m.y. *J.*
539 *Geophys. Res.* 93, 11569–11581.
- 540 Davies, C.J., Constable, C.G., 2014. Insights from geodynamo simulations into long-term geomagnetic field
541 behaviour. *Earth planet. Sci. Lett.* 404, 238–249.
- 542 De Santis, A., Barraclough, D., Tozzi, R., 2003. Spatial and temporal spectra of the geomagnetic field and
543 their scaling properties. *Phys. Earth Planet. Int.* 135, 125–134.
- 544 Dormy, E., 2016. Strong-field spherical dynamos. *J. Fluid Mech.* 789, 500–513. doi:10.1017/jfm.2015.747.
- 545 Finlay, C.C., Jackson, A., 2003. Equatorially dominated magnetic field change at the surface of Earth’s core.
546 *Science* 300, 2084–2086.
- 547 Finlay, C.C., Olsen, N., Gillet, N., Jault, D., 2013. Rapid core field variations during the satellite era: investi-
548 gations using stochastic processes based field models. AGU Fall meeting.
- 549 Fournier, A., Aubert, J., Thébault, E., 2015. A candidate secular variation model for IGRF-12 based on Swarm
550 data and inverse geodynamo modelling. *Earth, Planets and Space* 67, 81.
- 551 Fournier, A., Nerger, L., Aubert, J., 2013. An ensemble Kalman filter for the time-dependent analysis of the
552 geomagnetic field. *Geochem. Geophys. Geosyst.* 14, 4035–4043.
- 553 Frisch, U., 1995. *Turbulence: the legacy of AN Kolmogorov.* Cambridge University Press, Cambridge (UK).
- 554 Gardiner, C.W., 1985. *Handbook of stochastic methods for physics, chemistry and the natural sciences.*
555 Springer, Berlin.
- 556 Gillet, N., Barrois, O., Finlay, C., 2015. Stochastic forecasting of the geomagnetic field from the COV-
557 OBS.x1 geomagnetic field model, and candidate models for IGRF-12. *Earth, Planets and Space* 67, 71.
558 doi:10.1186/s40623-015-0225-z.
- 559 Gillet, N., Jault, D., Canet, E., Fournier, A., 2010. Fast torsional waves and strong magnetic field within the
560 Earth’s core. *Nature* 465, 74–77.
- 561 Gillet, N., Jault, D., Finlay, C.C., Olsen, N., 2013. Stochastic modelling of the Earth’s magnetic field: inversion
562 for covariances over the observatory era. *Geochem. Geophys. Geosyst.* 14, 766–786.
- 563 Greenspan, H.P., 1968. *The theory of rotating fluids.* CUP Archive.
- 564 Hellio, G., 2015. Stochastic modeling of archeomagnetic measurements. Ph.D. thesis. Université Grenoble
565 Alpes. URL: <https://tel.archives-ouvertes.fr/tel-01218123>.
- 566 Hellio, G., Gillet, N., Bouligand, C., Jault, D., 2014. Stochastic modelling of regional archaeomagnetic series.
567 *Geophys. J. Int.* 199, 931–943.
- 568 Holme, R., Olsen, N., 2006. Core surface flow modelling from high-resolution secular variation. *Geophys. J.*
569 *Int.* 166, 518–528.
- 570 Holme, R., Olsen, N., Bairstow, F., 2011. Mapping geomagnetic secular variation at the core–mantle boundary.
571 *Geophys. J. Int.* 186, 521–528.
- 572 Hulot, G., Bouligand, C., 2005. Statistical palaeomagnetic field modelling and symmetry considerations.

- 573 Geophys. J. Int. 161, 591–602.
- 574 Hulot, G., Le Mouél, J., 1994. A statistical approach to the Earth's main magnetic field. *Phys. Earth planet.*
575 *Int.* 82, 167–183.
- 576 Jackson, A., Jonkers, A.R.T., Walker, M.R., 2000. Four centuries of geomagnetic secular variation from
577 historical records. *Phil. Trans. R. Soc. Lond. A* 358, 957–990.
- 578 Jazwinski, A.H., 2007. *Stochastic processes and filtering theory.* Dover Publications, Mineola.
- 579 Kageyama, A., Miyagoshi, T., Sato, T., 2008. Formation of current coils in geodynamo simulations. *Nature*
580 454, 1106–1109.
- 581 King, E.M., Buffett, B.A., 2013. Flow speeds and length scales in geodynamo models: The role of viscosity.
582 *Earth planet. Sci. Lett.* 371, 156–162.
- 583 Korte, M., Constable, C., 2011. Improving geomagnetic field reconstructions for 0–3 ka. *Phys. Earth planet.*
584 *Int.* 188, 247 – 259.
- 585 Korte, M., Donadini, F., Constable, C., 2009. Geomagnetic field for 0-3 ka: 2. A new series of time-varying
586 global models. *Geophys. Geochem. Geosyst.* 10. doi:10.1029/2008GC002297.
- 587 Kuipers, J., Hoyng, P., Wicht, J., Barkema, G., 2009. Analysis of the variability of the axial dipole moment of
588 a numerical geodynamo model. *Phys. Earth planet. Int.* 173, 228–232.
- 589 Lesur, V., Wardinski, I., Rother, M., Mandea, M., 2008. GRIMM: the GFZ Reference Internal Magnetic Model
590 based on vector satellite and observatory data. *Geophys. J. Int.* 173, 382–394.
- 591 Lhuillier, F., Aubert, J., Hulot, G., 2011a. Earth's dynamo limit of predictability controlled by magnetic
592 dissipation. *Geophys. J. Int.* 186, 492–508.
- 593 Lhuillier, F., Fournier, A., Hulot, G., Aubert, J., 2011b. The geomagnetic secular-variation timescale in obser-
594 vations and numerical dynamo models. *Geophys. Res. Lett.* 38, L09306. doi:10.1029/2011GL047356.
- 595 Lowes, F., 1974. Spatial power spectrum of the main geomagnetic field, and extrapolation to the core. *Geophys.*
596 *J. R. astr. Soc.* 36, 717–730.
- 597 MacKay, 1998. Introduction to Gaussian processes, in: Bishop, C.M. (Ed.), *Neural networks and machine*
598 *learning,* Springer, Berlin. pp. 133–165.
- 599 Mandea, M., Holme, R., Pais, A., Pinheiro, K., Jackson, A., Verbanac, G., 2010. Geomagnetic jerks: rapid
600 core field variations and core dynamics. *Space science reviews* 155, 147–155.
- 601 Meduri, D.G., Wicht, J., 2016. A simple stochastic model for dipole moment fluctuations in numerical dynamo
602 simulations. *Front. Earth Sci.* 4, 38.
- 603 Olson, P., Christensen, U., Driscoll, P., 2012. From superchrons to secular variation: A broadband dynamo
604 frequency spectrum for the geomagnetic dipole. *Earth planet. Sci. Lett.* 319-320, 75–82.
- 605 Panovska, S., Finlay, C., Hirt, A., 2013. Observed periodicities and the spectrum of field variations in Holocene
606 magnetic records. *Earth planet. Sci. Lett.* 379, 88–94.
- 607 Percival, D.B., Walden, A.T., 1993. *Spectral Analysis for Physical Applications: Multitaper and Conventional*
608 *Univariate Techniques.* Cambridge University Press, Cambridge.
- 609 Riedel, K.S., Sidorenko, A., 1995. Minimum bias multiple taper spectral estimation. *IEEE Transactions on*

- 610 Signal Processing 43, 188–195.
- 611 Roberts, P., Jones, C., Calderwood, A., 2003. Energy fluxes and ohmic dissipation in the earth’s core, in: Jones,
612 C., Soward, A., Zhang, K. (Eds.), Earth’s core and lower mantle. Taylor & Francis, London, pp. 100–129.
- 613 Schaeffer, N., 2013. Efficient spherical harmonic transforms aimed at pseudospectral numerical simulations.
614 *Geochem. Geophys. Geosyst.* 14, 751–758.
- 615 Schaeffer, N., 2015. Exploring the physics of the Earth’s core with numerical sim-
616 ulations. Habilitation à diriger des recherches. Université Grenoble Alpes. URL:
617 <https://tel.archives-ouvertes.fr/tel-01241755>.
- 618 Soderlund, K.M., King, E.M., Aurnou, J.M., 2012. The influence of magnetic fields in planetary dynamo
619 models. *Earth planet. Sci. Lett.* 333, 9–20.
- 620 Takahashi, F., Shimizu, H., 2012. A detailed analysis of a dynamo mechanism in a rapidly rotating spherical
621 shell. *J. Fluid Mech.* 701, 228–250.
- 622 Tanriverdi, V., Tilgner, A., 2011. Global fluctuations in magnetohydrodynamic dynamos. *New Journal of*
623 *Physics* 13, 033019.
- 624 Thébault, E., Gallet, Y., 2010. A bootstrap algorithm for deriving the archeomagnetic field intensity
625 variation curve in the Middle East over the past 4 millennia BC. *Geophys. Res. Lett.* 37, L22303.
626 doi:10.1029/2010GL044788.
- 627 Thomson, D.J., 1982. Spectrum estimation and harmonic analysis. *Proceedings of the IEEE* 70, 1055–1096.
- 628 Van Kampen, N.G., 2007. *Stochastic processes in physics and chemistry*. Elsevier, Amsterdam.
- 629 Welch, P., 1967. The use of fast Fourier transform for the estimation of power spectra: a method based on time
630 averaging over short, modified periodograms. *IEEE Transactions on audio and electroacoustics* , 70–73.
- 631 Yaglom, A.M., 2004. *An introduction to the theory of stationary random functions*. Dover Publications,
632 Mineola.
- 633 Ziegler, L., Constable, C., Johnson, C., Tauxe, L., 2011. PADM2M: a penalized maximum likelihood model
634 of the 0–2 Ma palaeomagnetic axial dipole moment. *Geophys. J. Int.* 184, 1069–1089.

635 APPENDIX A: MAXIMUM LIKELIHOOD ESTIMATION OF LAW PARAMETERS FOR

636 τ_N AND R_N

637 Within the maximum likelihood approach developed by Lhuillier et al. (2011b), the Gauss coefficients
638 are assumed to be the result of a random Gaussian stationary process with a zero mean and a variance
639 that depends only on the degree n . Given these assumptions, Lhuillier et al. (2011b) showed that
640 the quantity $(\tau_n/\bar{\tau}_n)^2$ follows an F-distribution (also known as a Fisher-Snedecor distribution) with
641 $((2n+1)N_n, (2n+1)N_n)$ degrees of freedom, noted $F^{(2n+1)N_n, (2n+1)N_n}$, with $\bar{\tau}_n$ the expectation of
642 the time-scale τ_n and N_n the number of independent values in the Gauss coefficient time-series. N_n is
643 equal to 1 when τ_n is estimated from an instantaneous model or a model covering a time-period shorter

644 than $3\tau_n$. N_n equals $T/(3\bar{\tau}_n)$ for time-series of duration T longer than $3\tau_n$. Following Lhuillier et al.
645 (2011b), the probability of a law (δ, γ) given the observed time-scale τ_n^{obs} for degrees N_0 to N is :

$$646 \quad f(\delta, \gamma) = \prod_{n=N_0}^N F^{(2n+1)N_n, (2n+1)N_n} \left[\left(\frac{\tau_n^{obs}}{\delta n^{-\gamma}} \right)^2 \right] \quad (\text{A.1})$$

647 Because the likeliest value of the probability density function $F^{K,K}$ is $(K-2)/(K+2)$ for $K > 2$,
648 the maximum likelihood estimate of (δ, γ) are the parameters that provide the maximum value of :

$$649 \quad f(\delta, \gamma) = \prod_{n=N_0}^N F^{(2n+1)N_n, (2n+1)N_n} \left[\frac{(2n+1)N_n - 2}{(2n+1)N_n + 2} \left(\frac{\tau_n^{obs}}{\delta n^{-\gamma}} \right)^2 \right] \quad (\text{A.2})$$

650 The parameters (α, β) of equation 16 can be estimated using a similar approach. Within the
651 assumptions of Lhuillier et al. (2011b), the quantity $(2n+1)R/\bar{R}_n$ follows a χ^2 -distribution with
652 $(2n+1)N_n$ degrees of freedom, noted $G^{(2n+1)N_n}$. The likeliest value of the χ^2 probability density
653 function G^K is $K-2$ for $K > 2$. Therefore, the maximum likelihood estimate of (α, β) are the
654 parameters that provide the maximum value of :

$$655 \quad f(\alpha, \beta) = \prod_{n=N_0}^N G^{(2n+1)N_n} \left[\left((2n+1)N_n - 2 \right) \frac{R^{obs}}{\alpha \beta^n} \right] \quad (\text{A.3})$$

656 The probability density functions defined in (A.3) and (A.2) and shown in Fig. A1 and A2 for
657 simulation S0 display a single maximum showing that this method provides a unique result. Note
658 however that the parameter spaces delimited by the contour lines of the probability density functions
659 deduced from the different estimates may not overlap. This is the case for the two averaged estimates
660 of τ_n (Fig. A1a and A1b) suggesting that the assumption of zero mean for the Gauss coefficients is
661 not correct. The contour lines are elongated in an oblique direction showing that errors on parameters
662 are correlated (errors on one parameter can be compensated by errors on the other parameters). As
663 expected, the parameter space delimited by the contour lines is larger when using the instantaneous
664 estimates of \hat{R}_n and $\hat{\tau}_n$, which emphasizes that the estimated law is in this case less accurate.

665 **APPENDIX B: RELAXING THE HYPOTHESES $\beta = 1$ AND $\gamma = 1$**

666 Fits of R_n and τ_n in §3.2 have been obtained assuming the restricting hypothesis $\beta = \gamma = 1$ in
667 equation (16). Here, we discuss how those regressions are modified once relaxing these constraints.
668 This test is motivated by the derivation, from current geomagnetic field models, of larger (resp. lower)
669 values for γ (resp. β). In particular, regression of τ_n from recent geomagnetic field models for degrees
670 $n \geq 3$ gives $\gamma \simeq 1.45$ (Holme and Olsen 2006). A slightly lower value is obtained when including
671 degree 2 in the regression.

672 For all estimates of R_n and τ_n and each simulation, we searched for the parameters (α, β) and

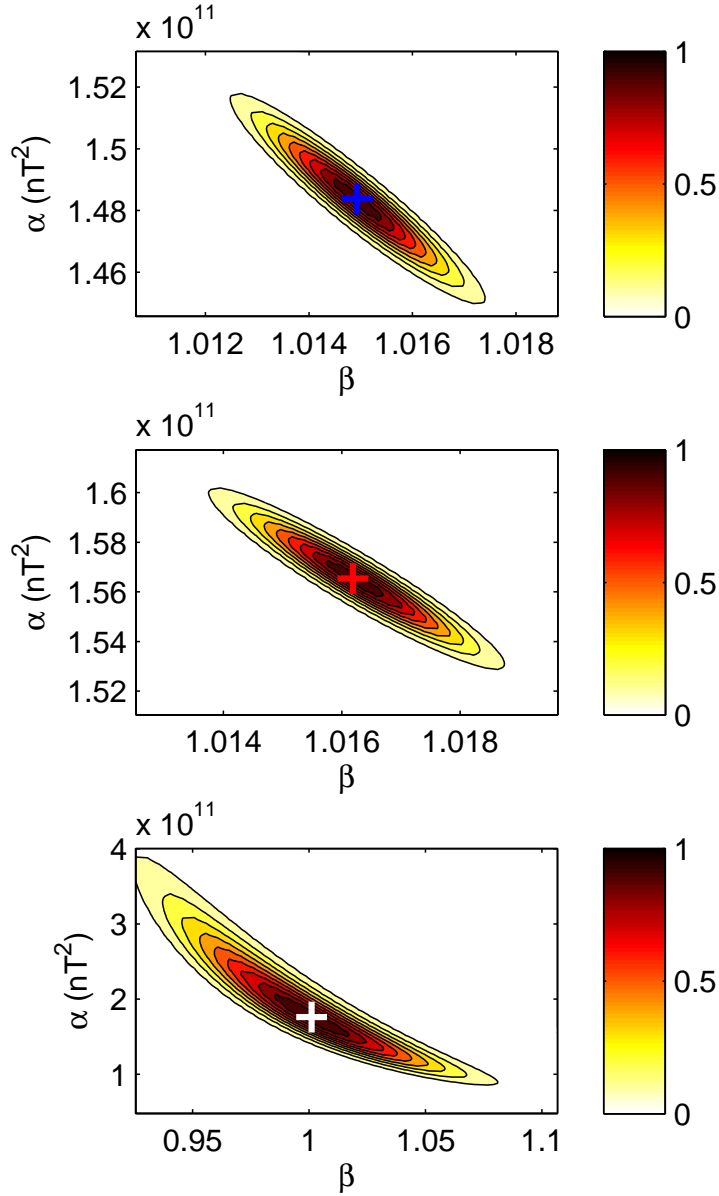


Figure A1. Probability density functions (normalized by their maximum value) for values of α and β (see equation 16) for the S0 simulation deduced from R_n^* estimated using Gauss coefficients after subtracting their averaged value (top), from \bar{R}_n using original Gauss coefficients (middle), and from an instantaneous \hat{R}_n (bottom). Crosses indicate the maximum likelihood parameters.

673 (δ, γ) from equation (16) for $n \in [2, 13]$. We used both the least-squares and the maximum likelihood
 674 methods. Results of the parameter search are summarized in Tables A1 and A2 and Fig. A3. As already
 675 observed by Lhuillier et al. (2011b), the results from the least-squares inversion and the maximum
 676 likelihood approach do not differ much.

677 The three simulations, run for different dimensionless parameters, provide different values of
 678 (α, β) and (δ, γ) . Both S0 and CE show almost flat CMB spectra ($\beta \simeq 1$), whereas R_n is slightly

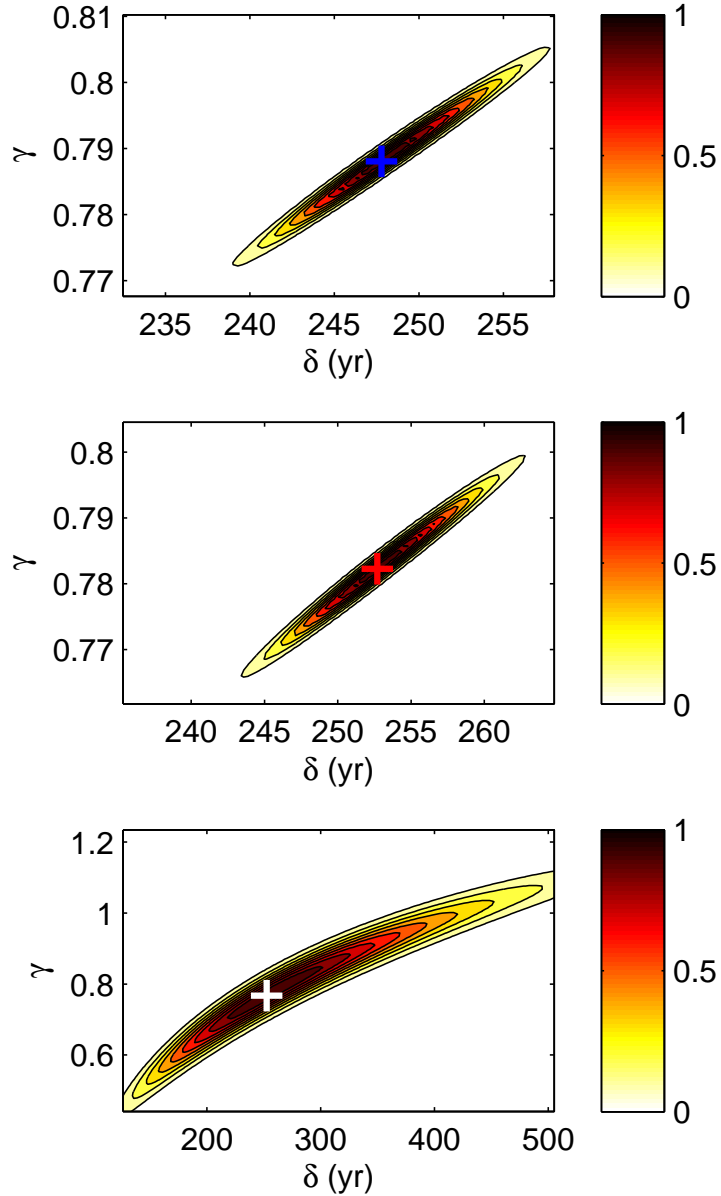


Figure A2. Probability density functions (normalized by their maximum value) for values of δ and γ (see equation 16) for the S0 simulation deduced from averaged τ_n^* estimated using Gauss coefficients after subtracting their averaged value (top), from $\bar{\tau}_n$ using original Gauss coefficients (middle), and from an instantaneous $\hat{\tau}_n$ (bottom). Crosses indicate the maximum likelihood parameters.

679 decreasing with n ($\beta \simeq 0.9$) for S1. The values of γ for our simulations range from 0.75 to 1.3 (from
 680 average spectra), encompassing the value $\gamma = 1$ favored by Lhuillier et al. (2011b) and found for
 681 the CE simulation. The most extreme (lowest viscosity, strongest forcing) simulation S1 shows the
 682 steepest decrease of τ_n with n (larger value of γ). S1 thus gives the closest value of γ to the instan-
 683 tantaneous estimate from geomagnetic observations. For CE and S1, γ is decreased by about 5% when
 684 removing the time-average Gauss coefficients in the estimations of R_n and τ_n . Despite its relatively

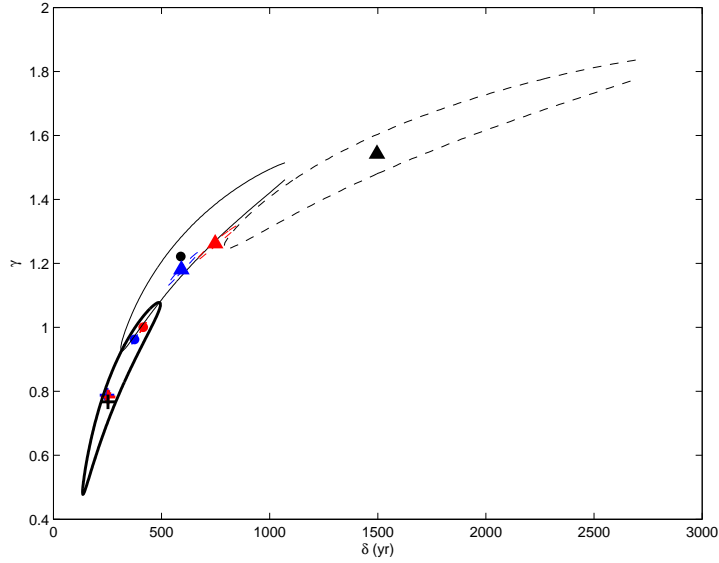


Figure A3. Curves of constant probability density (corresponding to 20% of the maximum probability) and maximum probability in the plane (δ, γ) obtained with the maximum likelihood method for one snapshot of each simulation S0 (black thick line and cross), CE (black thin line and filled circle), and S1 (black dashed line and triangle). For comparison, we also show the maximum probabilities from time-averages obtained while keeping (red) or not (blue) the average. Note that the probability functions obtained from time-averages are also represented but are restricted to too small parameter space to be visible on this figure.

685 modest forcing and viscosity and its specific torque and heat flux conditions, the simulation CE nev-
 686 ertheless presents a correlation time τ_n more sensitive to n than S0. Estimated values for δ encompass
 687 $\tau_{SV} = 415$ years (τ_{SV} is defined as δ for $\gamma = 1$). This time differs from τ_{SV} in the simulations S0 and
 688 S1, for which γ deviates significantly from 1, and it is close to τ_{SV} in the simulation CE for which
 689 $\gamma \simeq 1$.

690 If in average, parameters obtained from snapshot estimates \hat{R}_n and $\hat{\tau}_n$ are mostly similar to those
 691 obtained using time-averaged, a r.m.s. mismatch of about 20% (resp. 5%) may be found between
 692 instantaneous and time-integrated estimates of the parameter γ (resp. β) defining the dependence of
 693 τ_n (resp. R_n) with the degree n . From Table A2, the two-sigma intervals found for γ in simulations
 694 S0, CE and S1 are respectively $[0.45, 1.05]$, $[0.70, 1.3]$, and $[0.85, 1.7]$ using the maximum likelihood
 695 method of Appendix A. Similar ranges of values are obtained by computing the probability density
 696 function obtained from a single snapshot of τ_n , as illustrated in Fig. A3.

		α		β	
		LSQ	ML	LSQ	ML
S0	(a)	147.0 ± 107.5	156.1 ± 86.3	1.05 ± 0.07	1.03 ± 0.05
	(b)	152.6	156.5	1.02	1.02
	(c)	143.1	148.4	1.02	1.01
CE	(a)	10.2 ± 5.9	11.0 ± 5.3	1.00 ± 0.05	0.99 ± 0.04
	(b)	10.3	11.2	0.99	0.99
	(c)	8.6	9.7	1.01	1.00
S1	(a)	33.2 ± 16.6	42.5 ± 20.1	0.93 ± 0.04	0.91 ± 0.03
	(b)	37.5	37.7	0.91	0.91
	(c)	27.7	27.3	0.93	0.93

Table A1. Parameters (α, β) for simulations S0, CE and S1, estimated from the least-squares (LSQ) and maximum likelihood (ML) approaches. α is expressed in 10^9 nT^2 and β is dimensionless. (a) estimated from snapshot values \hat{R}_n (average value \pm standard deviation, for 10 independent epochs); and from the expected variances as in equation (15), either removing (c) or keeping (b) the average value of the coefficients.

		δ		γ	
		LSQ	ML	LSQ	ML
S0	(a)	$313 \pm 154(0.75 \pm 0.37)$	$278 \pm 128(0.67 \pm 0.31)$	0.81 ± 0.18	0.75 ± 0.15
	(b)	294(0.71)	253(0.61)	0.86	0.78
	(c)	284(0.68)	248(0.60)	0.85	0.79
CE	(a)	$500 \pm 153(1.20 \pm 0.37)$	$460 \pm 135(1.11 \pm 0.33)$	1.07 ± 0.16	1.02 ± 0.16
	(b)	461(0.97)	415(1.00)	1.05	1.00
	(c)	401(0.97)	375(0.90)	0.99	0.96
S1	(a)	$835 \pm 426(2.01 \pm 1.03)$	$939 \pm 409(2.26 \pm 0.99)$	1.22 ± 0.27	1.29 ± 0.22
	(b)	704(1.70)	748(1.80)	1.23	1.26
	(c)	585(1.41)	592(1.43)	1.17	1.18

Table A2. Parameters (δ, γ) for simulations S0, CE and S1, estimated from the least-squares (LSQ) and maximum likelihood (ML) approaches. δ is expressed in years (and in terms of τ_{SV} in parentheses) and γ is dimensionless. (a) estimated from snapshot values $\hat{\tau}_n$ (average value \pm standard deviation, for 10 independent epochs); and from the expected variances as in equation (15), either removing (c) or keeping (b) the average value of the coefficients.